Spring 5-2012

Mode Water in the Sea of Japan: A Study on the Reproducibility of Mode Water in the Data-Assimilating Regional Navy Coastal Ocean Model

Lea Kristen Locke
University of Southern Mississippi

The University of Southern Mississippi

MODE WATER IN THE SEA OF JAPAN: A STUDY ON THE REPRODUCIBILITY OF MODE WATER IN THE DATA-ASSIMILATING REGIONAL NAVY COASTAL OCEAN MODEL

by

Lea Kristen Locke

A Thesis
Submitted to the Graduate School
of The University of Southern Mississippi
in Partial Fulfillment of the Requirements
for the Degree of Master of Science

Approved:

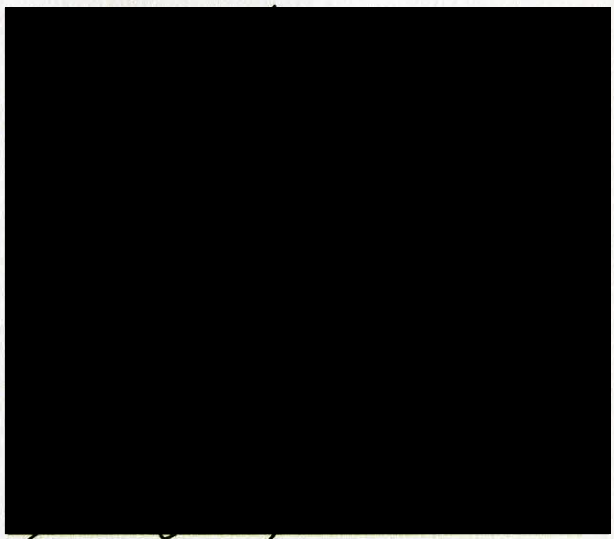

Dean of the Graduate School

May 2012

The University of Southern Mississippi

MODE WATER IN THE SEA OF JAPAN: A STUDY ON THE REPRODUCIBILITY OF MODE WATER IN THE DATA-ASSIMILATING REGIONAL NAVY COASTAL OCEAN MODEL

by

Lea Kristen Locke

Abstract of Thesis
Submitted to the Graduate School
of The University of Southern Mississippi
in Partial Fulfillment of the Requirements
for the Degree of Master of Science

May 2012

ABSTRACT

MODE WATER IN THE SEA OF JAPAN: A STUDY ON THE REPRODUCIBILITY OF MODE WATER IN THE DATA-ASSIMILATING REGIONAL NAVY COASTAL OCEAN MODEL

By Lea Kristen Locke

May 2012

Mode water in the Sea of Japan (SOJ) is associated with anti-cyclonic eddies that form in the quasi-stationary meanders of the offshore Tsushima Warm Current. Previous work in this region has shown free-running, advanced ocean models are able to capture the physical processes that generate mode water; however, data assimilation is seen to have a negative impact. A 3.5km resolution Regional Navy Coastal Ocean Model is used to assess the ability of a data-assimilating model to reproduce the mode water structure in the SOJ. The model's response to the assimilation of in-situ and synthetic profiles, derived from remotely sensed surface measurements, demonstrates that the model has difficulty recreating and retaining mode water beyond a single forecast run. The model's shortfall occurs because the climatological data, used to derive the synthetic profiles, are too coarse to capture the seasonal mode water evolution of the meander eddies. Two data analysis methods, EOF analysis and multi-variate regression analysis, are utilized to recreate synthetic profiles in the mean locations of the meander eddies during peak mode water occurrence months.

ACKNOWLEDGMENTS

I would like to thank my thesis advisor, Dr. Dmitri Nechaev, and my other committee members, Dr. Vladimir Kamenkovich and Dr. Stephan Howden, for their time, advice, and suggestions in support of this work. I would also like to thank the Naval Oceanographic Office for allowing me access to their data, as well as time to complete this study.

A special thanks goes to Dr. Michael Toner at the Naval Oceanographic Office who was always willing to listen and guide me toward the right path! The use of Dr. Toner's software package, which he developed, was also extremely helpful and greatly appreciated. His knowledge and insight have truly been invaluable to me throughout this work. Appreciation is also expressed to my co-workers at the Naval Oceanographic Office for all their support and encouraging words.

TABLE OF CONTENTS

LIST OF ILLUSTRATIONS

Figure

CHAPTER I

INTRODUCTION

Mode water is defined as a vertically homogenous layer situated within or near the top of the permanent pycnocline. It is found in every major ocean basin and is generally associated with the creation and subduction of deep winter mixed layers. The exact depth mode water occupies is determined by its formation location. (Hanawa and Talley, 2001). This mode water phenomenon is known to exist in the Sea of Japan (SOJ). Numerical modeling experiments have shown the ability of the physics of a Princeton Ocean Model (POM) based ocean model to capture the processes creating mode water in the SOJ (Hogan and Hurlburt, 2006), but the effects of data-assimilation on the model's ability to create and maintain the mode water structure in this area is unknown. Since data-assimilation is vital to the United States Navy Fleet (USNF) in depicting the most accurate state of the ocean, it is of great importance to quantify the ability of the Navy's operational, data-assimilating ocean model, the Regional Navy Coastal Ocean Model (R-NCOM), to accurately reproduce the structure and location of mode water layers in the world oceans. This study provides a brief introduction to mode waters in general, their formation mechanisms and spatial extent in the SOJ, as well as a more in-depth look at SOJ mode water modeling capabilities and prediction. The problems introduced into the model results by data-assimilation with respect to mode water are discussed. A new method is suggested and outlined for the reduction of these assimilation errors in the SOJ, with possible model application to other areas in the world's ocean exhibiting the mode water phenomenon.

CHAPTER II

BACKGROUND INFORMATION

Mode Water, Definition and Characteristics

Mode waters form vertically homogenous layers situated within or near the top of the permanent pycnocline and are viewed as thermostads/pycnostads in vertical profiles at a given location or as a thickening of isotherms/isopycnals in a vertical cross-section (Hanawa and Talley, 2001; McCartney, 1982). It is important to note that all water properties are homogenous in mode layers, including salinity; however, since temperature-only profiles are much more prevalent than T-S observations, a thermostad is a far easier parameter to work with than a halostad. Mode water layers are also usually associated with elevated oxygen content relative to neighboring water masses. Mode water has been identified using a host of parameters: minimum in vertical density gradients, minimum in temperature gradients, minimum in potential vorticity, as well as layer thickness between specific isotherms/isopycnals. Mode water has been recognized in every ocean basin, typically on the warm side of a current or front, and is distributed well beyond its formation regions (Hanawa and Talley, 2001).

There are two types of mode water: the sub-tropical variety and the sub-polar variety (McCartney, 1982). The main difference between the two is their characteristic densities. Sub-tropical mode water (STMW) tends to be a less dense water mass located in the upper to middle pycnocline, whereas sub-polar mode water (SPMW) tends to be a denser, middle to lower pycnocline water mass. STMWs are associated with the western boundary current extensions of sub-tropical gyres. Extensive work has been done studying Atlantic STMW, 18°C water (McCartney, 1982), associated with the Gulf

Stream Extension (Fig. 1a). Likewise, much work has also been done studying its Pacific counterpart, North Pacific Sub-Tropical Mode Water (NPSTMW) (Hanawa and Suga, 1995), associated with the Kuroshio Extension region (Fig. 1).

Mode Water, Formation Mechanisms

Mode water formation areas are found in regions that experience deep wintertime convection. Mode water layers originate as thick winter mixed-layers that are consequently subducted and advected away from their formation regions. STMWs, especially in the northern hemisphere, are intimately linked to large surface heat losses induced by dry, cold air outbreaks from nearby continents during the winter (Hanawa and Talley, 2001). Because mode water formation is linked to deep wintertime mixed-layer generation, mode water properties are controlled by temporal variations in air-sea interaction, heat transfer, and eddy activity in the formation area (Hanawa and Talley, 2001). This connection between mixed-layer and mode water is also the reason why mode waters show anomalously elevated oxygen content, i.e., they have been in recent contact with the surface. Although not a necessity, mode water formation areas generally occur in conjunction with oceanic fronts. Front locations represent areas where convection processes are enhanced and sloping isopycnals precondition the area for upper water mass subduction into the ocean's stratified interior (Hanawa and Talley, 2001). Two important mechanisms for inducing the subduction of these layers into the main pycnocline are (1) Stommel's Demon process enhanced with lateral induction (Price, 2001) and (2) frontogenesis (Spall, 1995; Lee et al., 2006).

As far back as 1939, Iselin noted that subduction of upper water masses into the thermocline is biased toward late winter water conditions. In 1979, Stommel presented a

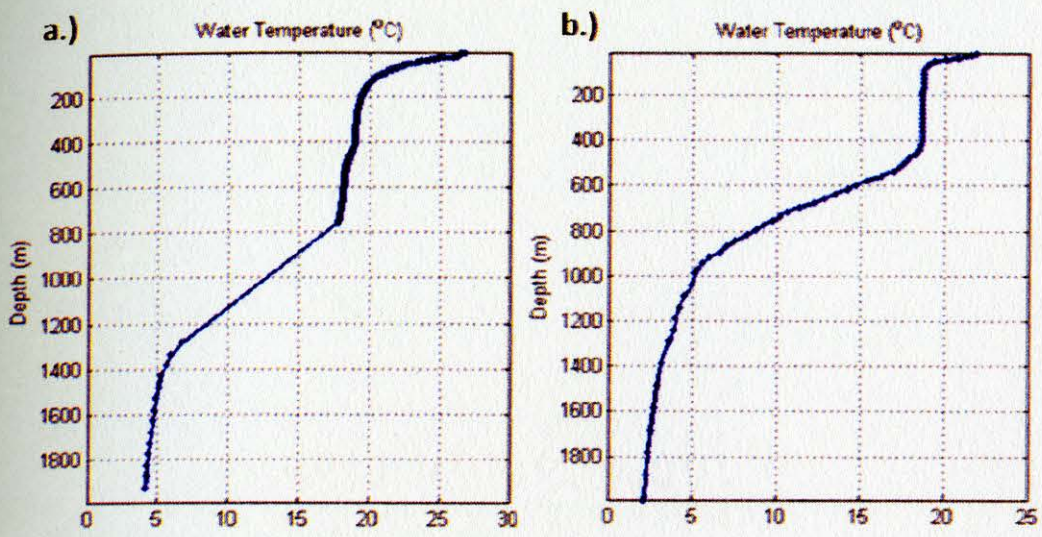

Figure 1. Example temperature profiles showing mode water in the Atlantic and Pacific Oceans. (*a*) Eighteen Degree mode water in the Atlantic Ocean Basin, and (*b*) of NPSTMW in the Pacific Ocean Basin.

simple model to explain this phenomenon known as the "Demon" model. In a region of convergent Ekman flow, like the subtropical gyres, there is downward Ekman pumping ($-\omega$). Considering an area where there is an isopycnal outcropping, the volume of water that is pumped downward must equal the volume of water that is subducted into the stratified interior (Fig. 2). Given that the latitudinal position of the outcrop varies significantly depending on the season, downward-pumped waters should also show significant variations in water properties as the front's position fluctuates. But, this is known not to be the case and the thermocline properties are more or less static and biased toward colder winter conditions. The reason for this is the temporal mismatch between the southward retreat of the outcrop and the downward Ekman pumping rate. The outcrop region retreats southward much faster than water is pumped downward. The deep layers created by the following winter overtake earlier pumped waters so that only the waters in

the lowest portions of the deep winter mixed layers are permanently subducted (Stommel, 1979).

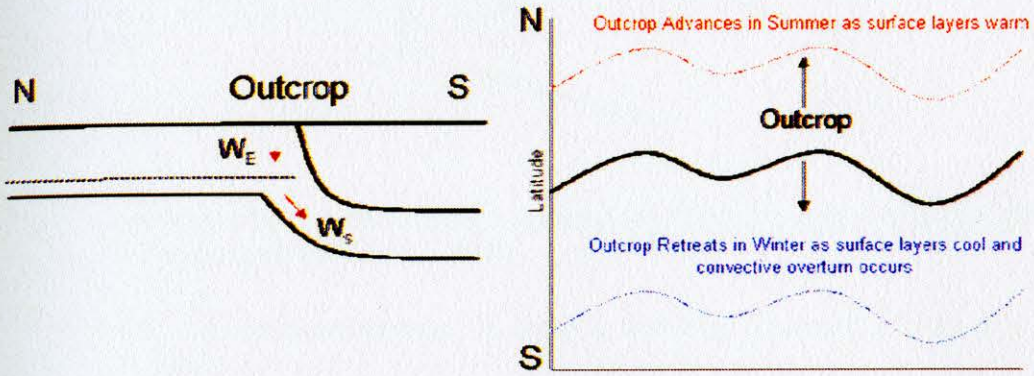

Figure 2. Schematic of subduction along isopycnal surfaces at an outcrop region with fixed mixed layer depth (Stommel, 1979).

By itself, Stommel's "Demon" model is not adequate to describe observed subduction rates in either the Atlantic or Pacific. Stommel's model assumes mixed layer depth to be fixed across the outcrop region. This assumption does not hold in many places. Mixed-layer depth variation across an outcrop region precludes the necessity for vertical water motion and indicates that horizontal flow can induce subduction into the thermocline (Fig. 3). This process has been termed "lateral induction" and, along with Stommel's "Demon," has been shown to play a major role in explaining the subduction rates observed in both the North Atlantic and North Pacific (Price, 2001).

While Stommel's "Demon" and lateral induction processes are viable mechanisms for inducing subduction at outcrop regions/oceanic fronts, internal processes unique to frontal zones are very important subduction mechanisms that can transport mode water layers into the ocean interior. The process of frontogenesis occurs when any part of a front develops an increased gradient, which can occur through meandering of

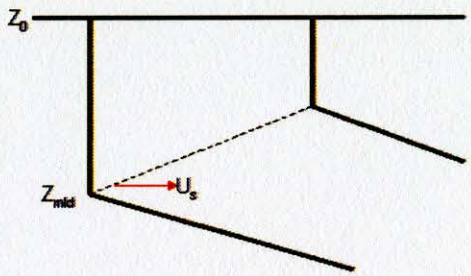

Figure 3. Schematic of subduction along isopycnal surfaces at an outcrop region with varying mixed layer depth (Williams, 1989).

the front or any other confluent process. In order to maintain geostrophic balance in the localized section of increased gradient, velocities must increase. The acceleration, given in equation (1), is compensated by cross-front ageostrophic flow, where v_a is the ageostrophic cross-front flow, and u_g is the geostrophic along-front flow. For a front

$$fv_a = \frac{Du_g}{Dt} \tag{1}$$

accelerating downstream ($Du_g/Dt>0$), an ageostrophic flow develops directed from the warm to cold side of the front ($v_a>0$). Also, as the acceleration occurs, cyclonic vorticity is increased on the cold side of the front, and anticyclonic vorticity is increased on the warm side due to increased shear. Conservation of potential vorticity requires horizontal flow to be convergent on the cyclonic side driving downwelling, and divergent on the anticyclonic side driving upwelling (Fig. 4). Continuity closes this cell with deep ageostrophic flow from the cold to warm side, which tends to subduct parcels from the surface layer into the interior (Fig. 5) (Spall, 1995).

A critical characteristic of frontal zones is the layer depth thickness of the outcropped isopycnal surface on the cold side of the front, which is often different from

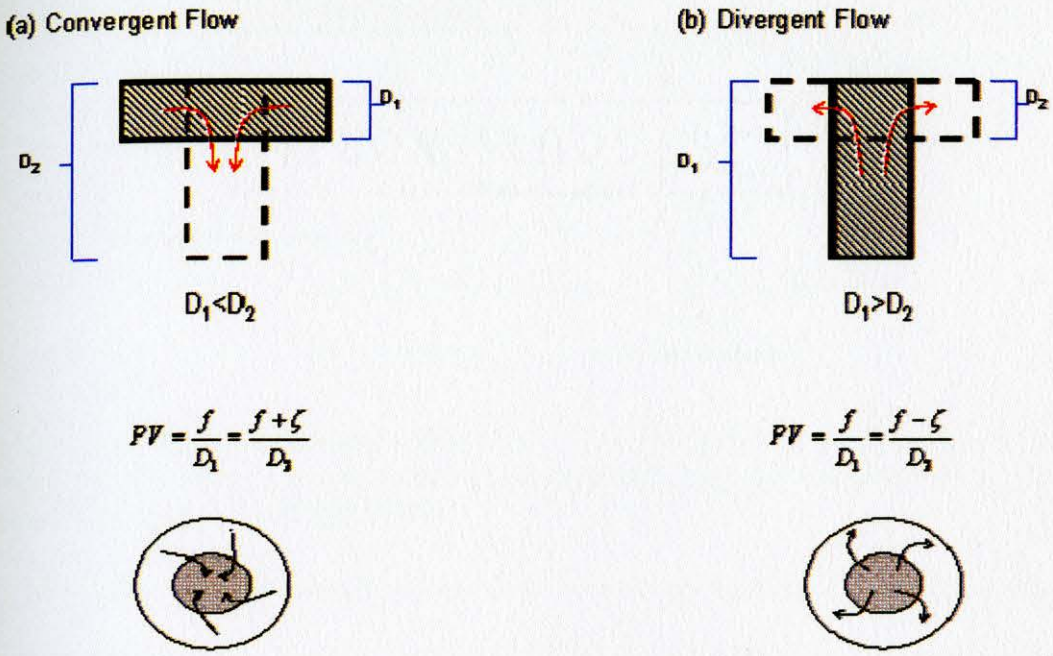

Figure 4. Schematic depicting concept of conservation of potential vorticity (Pond and Pickard, 1989).

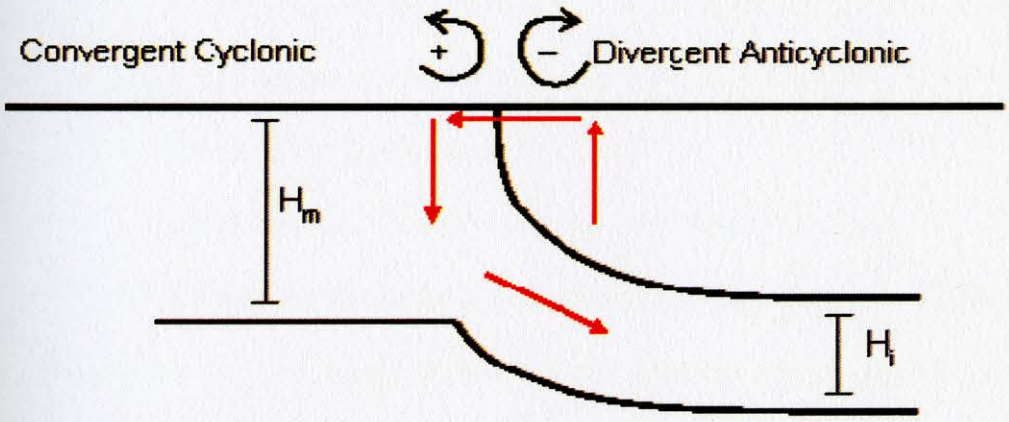

Figure 5. Schematic showing geostrophic and ageostrophic components produced during frontogenesis. Frontal dynamics induced subduction of surface layer waters where H_m is the mixed layer thickness on the cold side of the front and H_i is its corresponding isopycnal layer thickness on the warm side of the front (Spall, 1995).

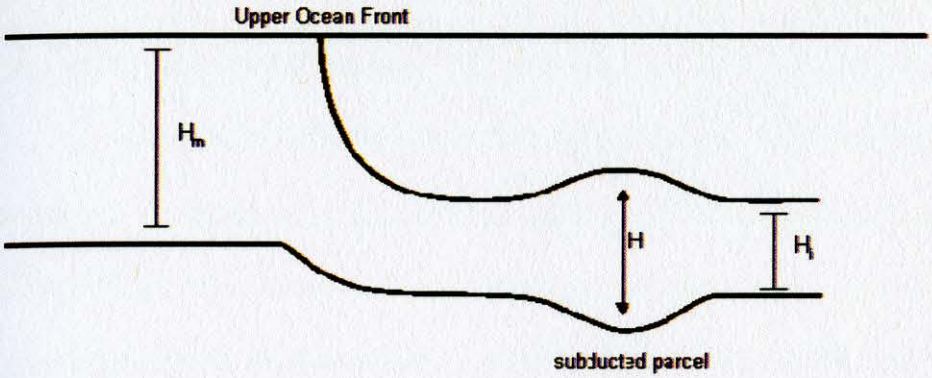

Figure 6. Schematic of an upper ocean front. H_m is the surface layer thickness, H_i, is the same isopycnal layer thickness in the stratified interior, and H is the thickness of the subducted water parcel (Spall, 1995).

the thickness of the corresponding isopycnal layer on the warm side of the front (Fig. 6). Spall showed that if the thickness of the subducted layer, H_m, is sufficiently larger than the thickness of its corresponding isopycnal layer, H_i, in the stratified interior, H_m will compress and acquire negative relative vorticity. The opposite is true for H_m, which is sufficiently smaller than H_i. This condition explains why many mode water layers are associated with anticyclonic circulations known as Intrathermocline Eddies (ITEs). ITEs are unique in that they display a lens-shape, having a domed top and bowled bottom (Kostianoy and Belkin, 1989; Gordon et al., 2002).

Sea of Japan, Basin Overview and Mode Water Formation

The Sea of Japan (SOJ) is a semi-enclosed sea reaching depths of ~3500m in its deepest parts. The sea is composed of three major basins, the Ulleung Basin in the southwest, the Yamato Basin in the southeast, and the Japan Basin in the north. The Ulleung and Yamato Basins are separated by the large Yamato Rise (Fig. 7). Inflow to the basin connecting the SOJ to the Pacific occurs through the Tsushima Strait with a sill depth of ~200m. Inflow through the Tsushima Strait shows seasonal variation, with

minimum transport seen in the winter through spring months and maximum transport seen in the summer through fall months. The mean transport through this strait is about 2Sv with a seasonal variation of about 1.3Sv (Preller and Hogan, 1998; Perkins et al., 2000; Nechaev et al., 2005). More than half the outflow to the Pacific flows through the Tsugaru Strait with a sill depth of ~130m. Outflow measurements taken in the Tsugaru Strait show varied results but most report an outflow between 1Sv and 2Sv with variable seasonal influence; this is likely due to the strong dependence of Tsugaru outflow on the inflow through the Tsushima Strait (Preller and Hogan, 1998). Flow through the Soya Strait to the Sea of Okhotsk with a sill depth of ~50m comprises the remaining outflow from the SOJ. Transport through the Soya strait is thought to be 1Sv or less, with maximum outflow occurring during the summer. Outflow through the Tatar Strait with a sill depth of ~10m is often considered negligible (Preller and Hogan, 1998).

Circulation in the SOJ is driven primarily by winds, thermohaline forcing, tides and throughflow; however, the circulation is controlled by bottom topography (Fig. 8) (Mooers et al., 2006). The circulation south of the Sub-Polar Front (SPF) is dominated by the eastward-flowing branches of the Tsushima Warm Current (TWC). The branches of the inflowing TWC are: (1) the East Korean Warm Current (EKWC), (2) the Nearshore Branch of the Tsushima Warm Current (N-TWC), and (3) the Offshore Branch of the Tsushima Warm Current (O-TWC). The EKWC flows along the Korean Peninsula bringing warmer, saline waters northward. The N-TWC flows along the coast of Honshu, and the O-TWC can be seen as the meandering EKWC as it separates from the coast. The meanders of the O-TWC are quasi-stationary and thought to be controlled by bathymetric features such as the Oki Spur and the Noto Peninsula (Mooers et al., 2006). The SOJ

basin circulation north of the SPF is cyclonic. Colder, fresher waters flow southward along the Primorye Coast as the Liman Cold Current (LCC). Once the LCC passes Peter the Great Bay (PGB), it is known as the North Korean Cold Current (NKCC). The NKCC and the EKWC meet between 37-40°N, where they leave the coast and flow eastward forming the SPF and its associated current. The Soya Warm Current (SWC) flows northward along the coast of Hokkaido and Sakhalin, closing the counterclockwise circulation. It is interesting to note that volume transport in the basin is ~20Sv, while the throughflow is only ~2Sv (Preller and Hogan, 1998).

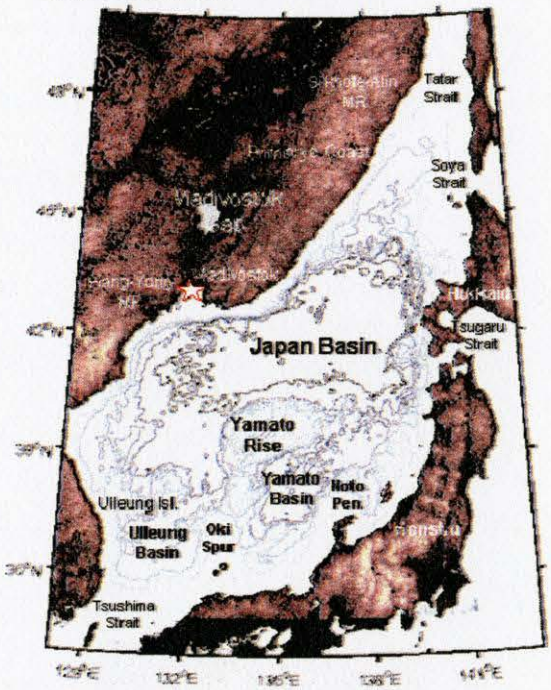

Figure 7. Bathymetric/Topographic overview of the basin.

Considering the shallow sill depths, the basin is almost completely isolated below 200m. So, it is surprising that the SOJ is the most ventilated region of the North Pacific with oxygen levels close to those seen in bottom water formation regions in the North

Atlantic (Talley et al., 2003). Two processes in the basin are responsible for the high oxygen levels, (1) brine rejection occurring in the northern portions of the sea, and (2) convection associated with winter cold-air outbreaks. While brine rejection is important for the deepest bottom water renewal and integral for residence time calculations, it is not a process involved in mode water formation, so it will not be discussed in any further detail. Winter convection, on the other hand, ventilates mid-depth waters and is intimately linked to mode water formation in the SOJ. During the winter months, primarily December through February, the SOJ is subject to periodic bursts of strong, dry, cold continental winds coming from the northwest. These cold-air outbreaks induce convection that may reach up to 1000m south of PGB. Convection is also vigorous near the SPF, where the contrast between air temperature and SST is large (Dorman et al., 2006; Talley et al., 2003; Lee et al., 2006). The deep mixed layers produced near the SPF

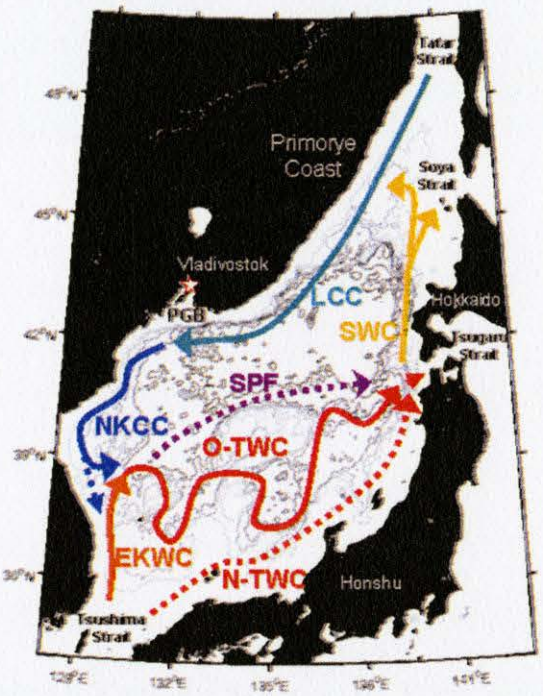

Figure 8. General circulation patterns in the SOJ basin.

in the winter are those that are subsequently subducted to form mode waters south of the front (Fig. 9). It is thought that frontogenesis is the main mechanism inducing subduction along the SPF (Lee et al., 2006). But, there are other external forcings that may enhance or induce subduction along the SPF in the SOJ. The wind associated with cold-air outbreaks, for example, has a significant along-front component driving Ekman flow from the cold to warm side of the front, which creates an unstable situation injecting cold, dense waters into the stratified interior (Lee et al., 2006). Not surprisingly then, winds and specifically cold-air outbreaks were found to be an important component in SOJ mode water creation by several numerical studies (Hogan and Hurlburt, 2006; Mooers et al., 2006).

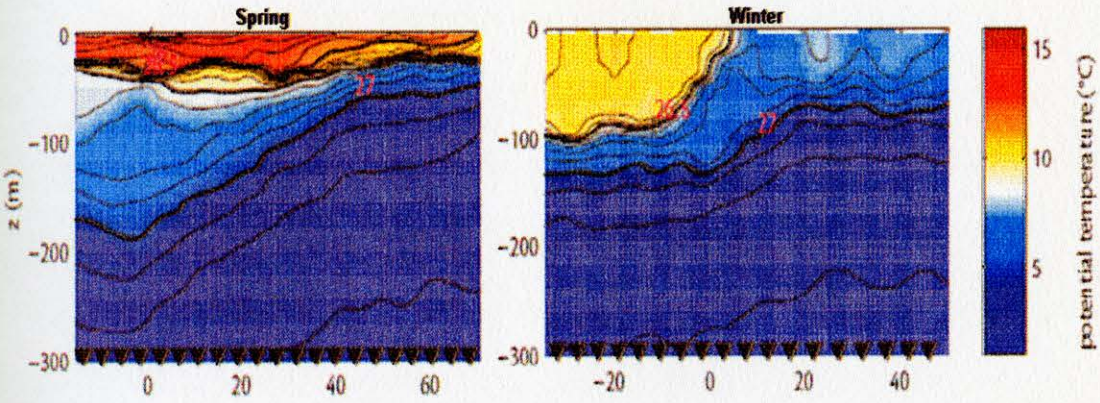

Figure 9. N-S temperature cross section across the SPF taken during the summer. Taken from SeaSoar surveys across the SPF during May 1999 (left) and January 2000 (right) (Lee et al., 2006).

Sea of Japan, Mode Water Characteristics and Spatial Patterns

The mode water found in the SOJ is a result of subduction of thick winter surface layers southward beneath the SPF as discussed earlier. These layers are generally between 9-11°C (26.5-27kg/m^3) and sit roughly between 100-300m water depth. To determine spatial patterns, ten years of public releasable data from the Master

Oceanographic Observation Data Set (MOODS) were extracted in the SOJ and analyzed for mode water layers. To ensure adequate resolution, only profiles containing five data points or more were retained for further analysis. Of the data extracted, ranging from 01/01/2000 – 08/14/2010, 12,948 profiles were analyzed (Fig. 10). Mode layers are determined using stratification ($\partial\rho_\theta/\partial z$) as the parameter of choice. For this study, a mode water profile is defined as a profile containing an interval of weak stratification (less than 0.005kg/m^3 change in density) located somewhere between the bottom of the mixed layer to the bottom of the thermocline. The minimum stratification layer is also restricted to have temperature properties above 5°C and be at least 30m thick to be classified as a mode water profile.

Of the 10-year dataset, 900 mode water profiles were identified. From Fig. 11, it can be seen that the mode water layers in the SOJ show peak occurrence in the spring and summertime months. Lowest occurrence of mode water is seen in the winter months and is attributed to the frequent Cold-Air Outbreaks experienced in the area that drive convection and mixed layer deepening to ~300m eroding mode water layers (Dorman et al., 2006; Hogan and Hurlburt, 2006). Also obvious, the mode water profiles are generally clustered around the quasi-stationary meanders of the O-TWC, which are known to seasonally transform into ITEs (Gordon et al., 2002; Hogan and Hurlburt, 2006). One interesting thing to note is the considerable amount of spread in the mode water temperature characteristics (Fig. 12). Mean temperature of the mode water layer is 10.7°C with a standard deviation of 1.8°C, almost a 4°C range in average temperature. This could be attributed to two things: (1) Since mode water layers are linked to deep mixed-layer formation, the variability could be due to the variations in wintertime

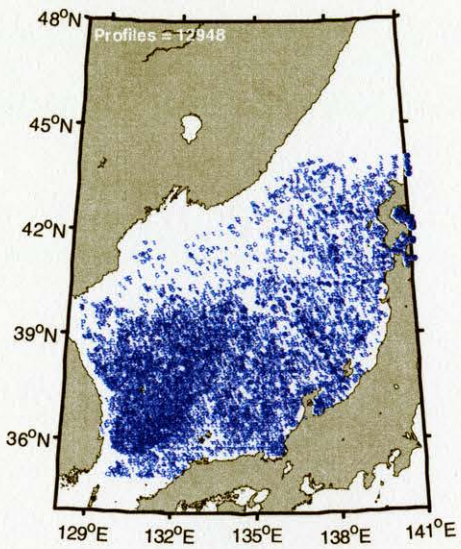

Figure 10. Spatial distribution of the ten-year MOODs dataset analyzed for mode water profiles in the SOJ.

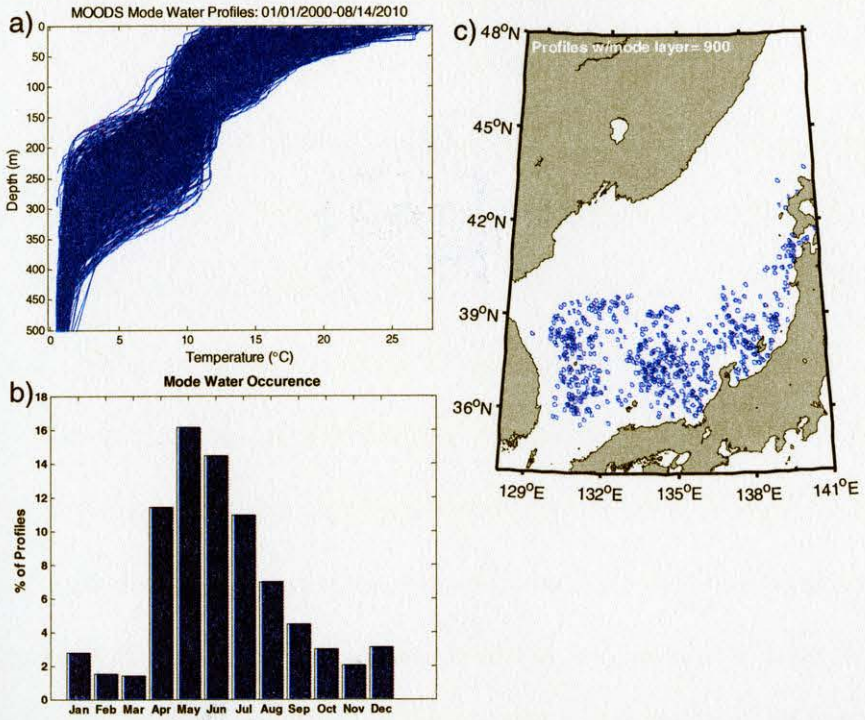

Figure 11. Characteristics and patterns of the mode water layers identified from the ten-year MOODS dataset. (a) T-Z plot of mode profiles, (b) monthly occurrence, (c) spatial distribution of mode water occurrence.

conditions experienced at the time of mixed-layer formation and subduction; alternatively, (2) there may be significant diapycnal mixing occurring as mode layers are subducted and then advected away, which is shown to play a role with Atlantic STMW (McCartney, 1982).

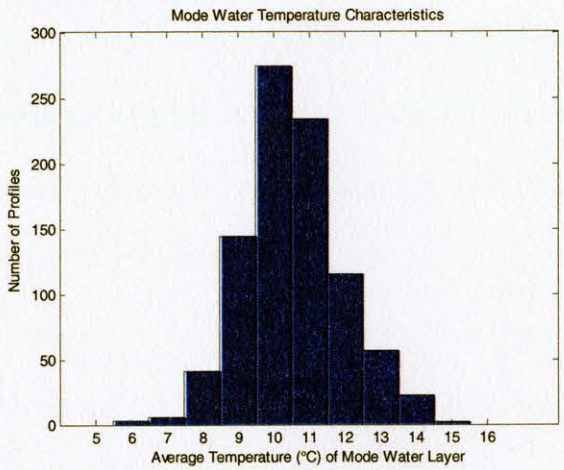

Figure 12. Average water temperature of mode layers in the ten-year MOODS data.

Sea of Japan, Ocean Model Description

The model used in this study is the Regional Navy Coastal Ocean Model (R-NCOM), which has a 1/32° (~3.5km) horizontal grid resolution. R-NCOM is a data-assimilating four-dimensional dynamic model based on the Princeton Ocean Model (POM). Model results are calculated using 50 vertical levels, 35 of which are σ-surfaces in shallow waters and the rest are z-levels. The σ-surfaces in the upper water column provide higher vertical resolution capable of resolving important smaller scale processes. In especially shallow waters, the σ-surfaces proportionally divide the distance between the ocean surface and bottom. Model output, however, is limited to 40 standard z-levels. Bathymetry and coastlines are from the Naval Research Laboratory (NRL) 2-minute Digital Bathymetric Data Base (DBDB) data set. Model output is in 3-hr increments and

forecasts extend out to 96 hours (4 days). The model domain spans 105°E to 148°E longitude and 7°N to 53°N latitude. The Sea of Japan (SOJ) lies fully inside the domain, and an adequate buffer exists between the basin and model edges to prevent boundary effects from contaminating model results in the region of interest.

Atmospheric forcing is provided by Fleet Numerical Meteorology and Oceanography Center's (FNMOC's) Coupled Ocean Atmosphere Mesoscale Prediction System (COAMPS), which comprises 10-meter winds at 15-km resolution, infrared heat flux, solar radiation, surface air pressure, dew point and dew pressure, and 2-meter air temperature. Fresh water input is provided from a subset of the World Meteorological Office (WMO) river database. At its open boundaries, R-NCOM is forced with Global Navy Coastal Ocean Model (G-NCOM) conditions as well as receiving tidal forcing from the Oregon State University (OSU) global tidal database.

R-NCOM is coupled with the Navy Coupled Ocean Data Assimilation (NCODA) System, which assimilates altimeter Sea Surface Height (SSH), satellite Sea Surface Temperature (SST) and in-situ profile observations. Based on the observational information received, NCODA creates a three-dimensional increment field, using a Multi-Variate Optimal Interpolation (MVOI) scheme, which is used to modify R-NCOM's initial conditions. If remotely sensed data are assimilated and the errors between the data and the previous model run are significantly different (Δ2cm SSH/Δ0.2°C SST), the surface increment is propagated into the subsurface through a "synthetic" profile. The information used to create the synthetic profiles is obtained from the Modular Ocean Data Assimilation System (MODAS). MODAS, in this particular usage, is a dynamic climatology created from historical temperature and salinity profiles

taken from the Master Oceanographic Observation Data Set (MOODS) database. In particular, information correlating the surface temperature and dynamic height to subsurface temperatures can be obtained. This correlation is achieved using empirical orthogonal functions (EOFs) to project surface information downward. In the case of MODAS, the regression coefficients obtained from the EOF analysis are direct linear relationships between SST, Sea Surface Height (SSH) and temperature at a given depth. The regression coefficients are stored bimonthly and exist on a variable grid spacing not exceeding 1/8° (15-km) in the SOJ (Fox, 2002).

Sea of Japan, Mode Water Forecast Predictability

It was shown by Hogan and Hurlburt (2006) that the Hybrid Coordinate Ocean Model (HYCOM) is able to reproduce mode water structure in the SOJ. Although a different numerical model, HYCOM is very similar to R-NCOM. Both are hydrostatic primitive equation ocean circulation models with similar resolutions. So, the physics behind R-NCOM should also be adequate to produce mode water in the SOJ. The major difference between the two models is HYCOM did not assimilate data in the Hogan and Hurlburt experiment while R-NCOM assimilates data in real-time. As seen in Fig. 13 there is high correlation between R-NCOM's placement of the meander ITEs and the location of the summer 2010 mode water locations. However, the eddy's observed vertical structure and the modeled vertical structure is vastly different (Fig. 14). While the mean R- NCOM temperature section does not show the mode structure of the ITEs, synoptically the model is able at times to "pull" toward the mode layer if a mode water profile is assimilated. Two profiles were assimilated in the Yamato Eddy (YE), which is

centered at 134°E, during 06/22/2010 – 06/30/2010. The effect the profiles had on the model is shown in Fig. 15.

It is easily seen that the assimilation of mode profiles significantly changes the model's vertical structure (Fig. 16), where the YE looks most "mode-like" on 06/25 and 06/26 after the mode profiles had been ingested. After assimilation of the profiles, the mode layer in the YE is steadily degraded until it is completely eroded by 06/30. Another interesting thing to note is the structure of the Ulleung Eddy (UE) (Fig. 16); it never looks to contain a mode signature, and coincidentally it is the only one of the meander ITEs not to have an in-situ mode profile assimilated during this time period. This suggests R-NCOM relies heavily upon assimilation of real-time mode water observations for mode water creation that it cannot maintain in the absence of data.

Sea of Japan, Synthetic Profiles

While the model is able to pull toward the mode layers once data are ingested, the synthetic profiles, which are created when there is a significant difference between remotely sensed data and the model background, do not contain any mode water signature (Fig. 17). So, mode water the model was able to reproduce by assimilating in-situ data is completely wiped out once a synthetic profile is created in a meander ITE. Even in the best case scenario where errors associated with remotely sensed data are nil, the synthetic profiles are still unable to replicate mode layers (Fig. 18).

There are several reasons for the synthetics shortcomings in the SOJ. As mentioned earlier, the regression coefficients used to compute the synthetic profiles were created with a spatial resolution no greater than 1/8° (15-km) in the SOJ (Fox, 2002; Carnes et al., 1994). The spatial scales of the meander ITEs are about 50-100km, possibly

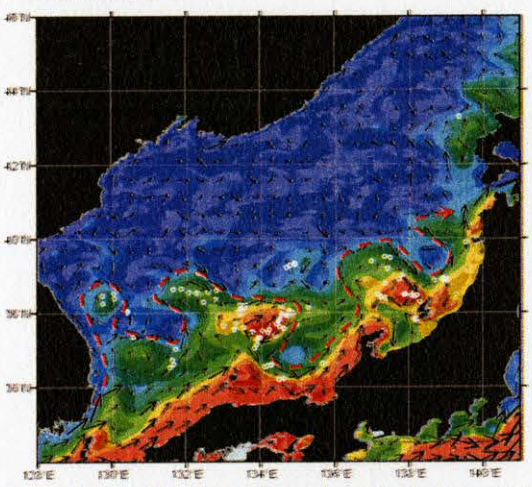

Figure 13. Summer 2010 mode profile locations in relation to R-NCOM's eddy field. R-NCOM mean SSH overlaid with mean surface currents from 06/22/2010 - 06/30/2010 (background), summer 2010 mode water profile locations from the MOODS dataset (white circles), and the approximate location of the O-TWC as inferred from the modeled SSH (red dashed line).

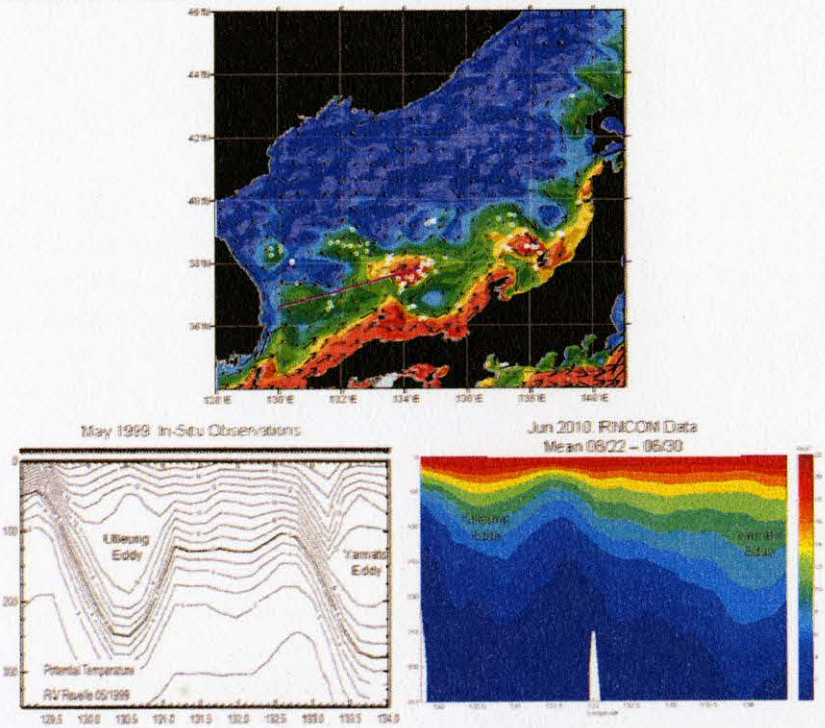

Figure 14. Vertical temperature structure of in-situ versus modeled Ulleung and Yamato ITEs. Pink line in the top panel shows the approximate cross section taken in the bottom panels. SeaSoar data taken from the RV Revelle in May 1999 (bottom-left) (Gordon et al., 2002). Mean RNCOM temperature data from 06/22/2010 - 06/30/2010 (bottom-right).

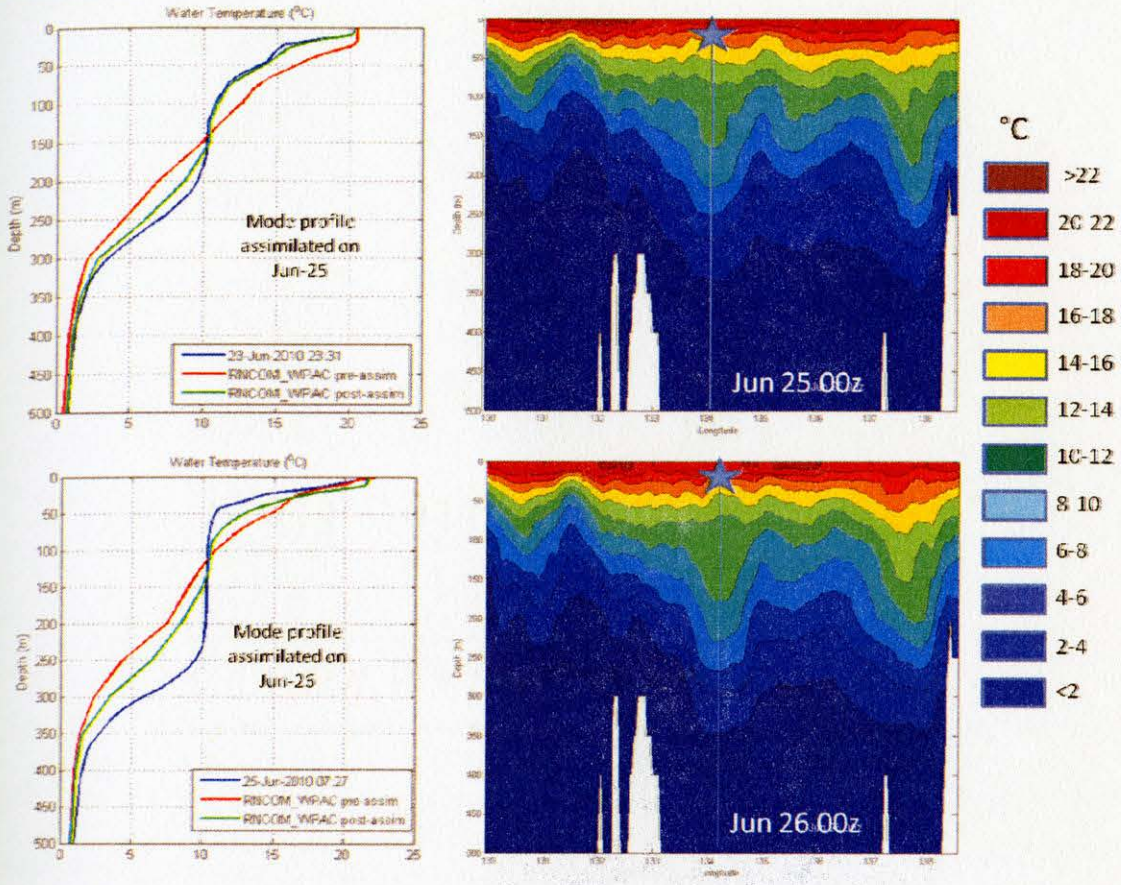

Figure 15. Assimilation effects of in-situ mode water profiles on the RNCOM vertical eddy structure. Left panel: In-situ mode profiles (blue) assimilated in the Yamato Eddy, along with the modeled profiles before (red) and after (green) assimilation. Right panel: R-NCOM temperature cross section of the Yamato Eddy (centered around 134-135E) after assimilation of in-situ profiles. Starred location on the cross section gives the approximate location of the in-situ profile.

too small for mode layers to be resolved by the synthetics. Temporal scales are also a problem. Mode layers are most prominent from April through July, and regression coefficients were determined bimonthly. Mode water is a higher vertical mode phenomenon, while synthetic profiles were created using only three vertical modes describing variability of temperature (Carnes et al., 1994). The nature of the structure in the meander ITEs, domed top and bowled bottom, creates a situation where the SSH

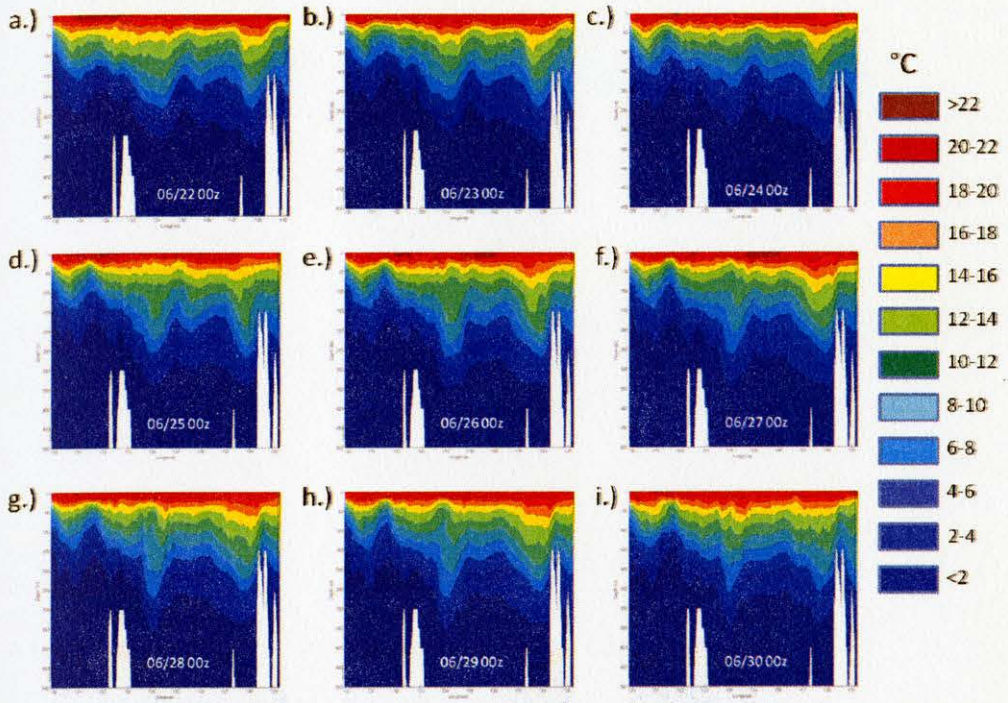

Figure 16. Timeseries snapshots at model initialization of ITE vertical structure. Panels (a) - (i) show the time progression of a temperature cross section through the meander ITEs. The Ulleung Eddy (UE) is centered between 130-131E, the Yamato Eddy (YE) is centered ~134E, and the Western Honshu Eddy (WHE) is centered ~137E. Note contours on all graphics are at 2°C intervals and all color scales are the same.

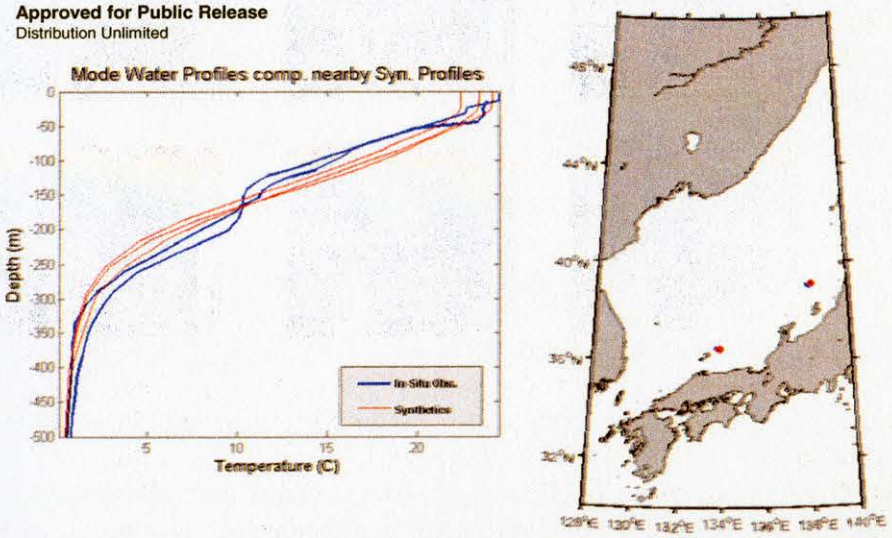

Figure 17. In-situ mode water profiles compared to nearby synthetic profiles. In-situ mode profiles taken in the beginning of October 2010 (blue) and synthetic profiles (red) assimilated very near the observed time and location of the in-situ profiles. Right panel shows the spatial location of the in-situ (blue) and synthetic (red) profiles.

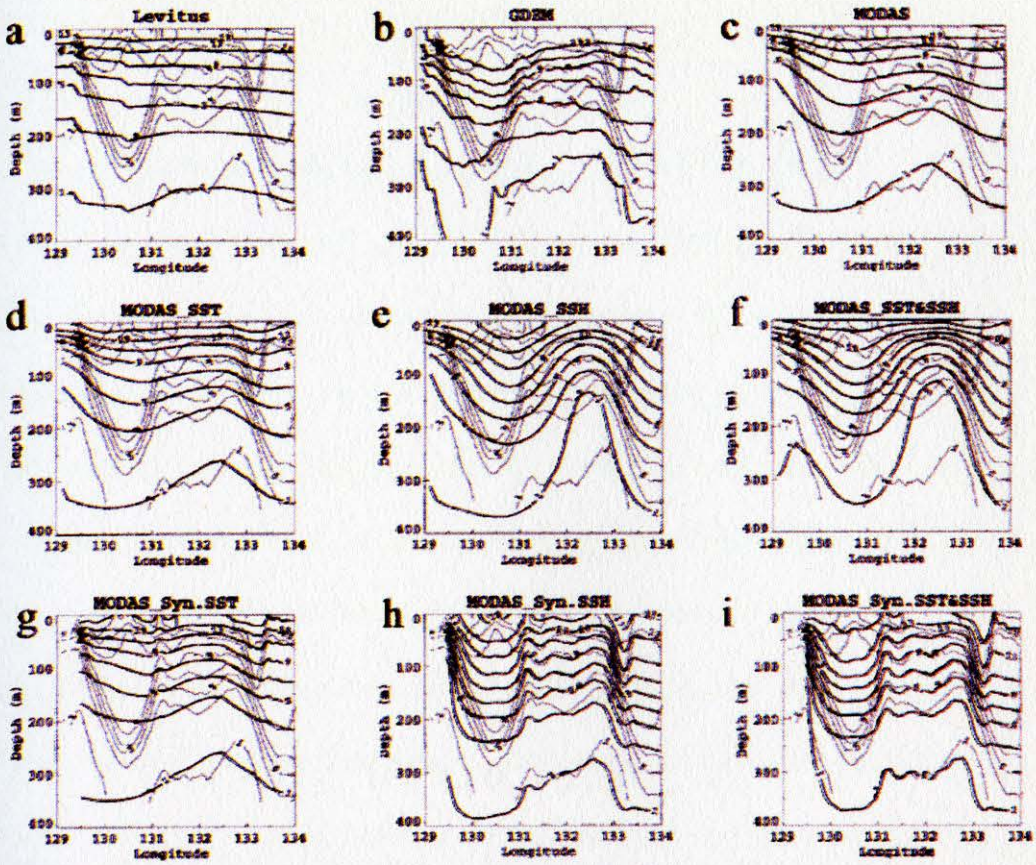

Figure 18. Three different synthetic climatologies, GDEM, Levitus, and MODAS compared to in-situ data. Thin lines in panels are temperature contours from SeaSoar data transecting meander ITEs. Bold lines are synthetic profiles created from static and dynamic climatologies. Top row: Synthetics are derived from three static climatologies. Middle row: Synthetics are derived from dynamic climatologies where remotely sensed SST and SSH are used to determine profile shape. Bottom row: Synthetics are also derived from dynamic climatology, but the information used for SST and SSH comes from the SeaSoar data and represents the best case scenario for synthetic creation (no measurement errors associated with satellite measurements) (Fox, 2002).

the meander ITEs, domed top and bowled bottom, creates a situation where the SSH signature is ~10cm less than would be expected from the linear relationship of thermocline to sea-level (Gordon et al., 2002). In addition to all these reasons, altimetry errors are estimated to be large in the SOJ because of the poor tidal corrections along with errors introduced by the barotropic motions known to propagate around the basin, although recent advances in altimetry processing has lead to increased accuracy of altimeter observations in enclosed seas (Morimoto et al., 2000; Xu et al., 2007, 2008).

CHAPTER III

OBJECTIVE OF STUDY

Since it has been shown that the synthetic profiles in the SOJ do not contain a mode water signature, it is believed that their assimilation into R-NCOM causes the model's inability to create and maintain mode water inside the ITEs. Also, since the model domain is large and encompasses more than just the SOJ, we are unable to turn off synthetic generation in only this region. In addition to this, it is the synthetics that deliver remotely sensed information to the model. Turning synthetic generation off would severely limit the amount of observation data R-NCOM receives and would likely negatively impact other areas of model performance, like accurate model placement of fronts and eddies. Because of these reasons, it is concluded that in order to improve model performance in the SOJ, with respect to mode water structure, the area's synthetic profiles must be reworked. Deriving a method for the creation of synthetic profiles in the SOJ which captures the mode water signature, will more adequately depict the meander ITEs vertical structure while also allowing the assimilation of remotely sensed data to continue in the model without adverse effects.

CHAPTER IV

DATA OVERVIEW

Since only synthetics in the vicinity of the quasi-stationary ITEs during a certain timeframe need to be recalculated, a larger dataset is desired in order to maximize the chance of capturing the interannual variability of ITE locations and mode water characteristics, as well as obtaining the most data possible to perform further analyses. For these reasons, another MOODS extraction was done spanning 1900-2010. Approximately 61,457 profiles were extracted and analyzed for mode water (Fig. 19). Of the 60,000+ profiles, 4415 mode profiles were identified (Fig. 19). The locations of mode water profiles from the larger dataset look similar to the patterns seen from the 2000-2010 dataset (Fig. 11c), clustered around mean ITE locations but showing a wider distribution south of the SPF. A mode water frequency map was determined from the

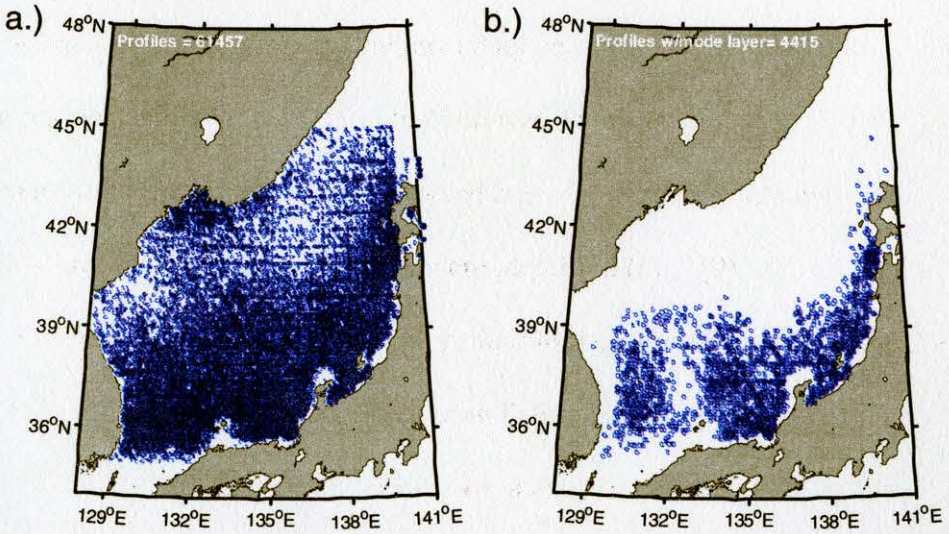

Figure 19. Location plots of all profiles and mode water profiles from the 1900-2010 dataset. (*a*) Location map of the all profiles from the 1900-2010 dataset, and (*b*) location map of all mode water profiles from the 1900-2010 dataset.

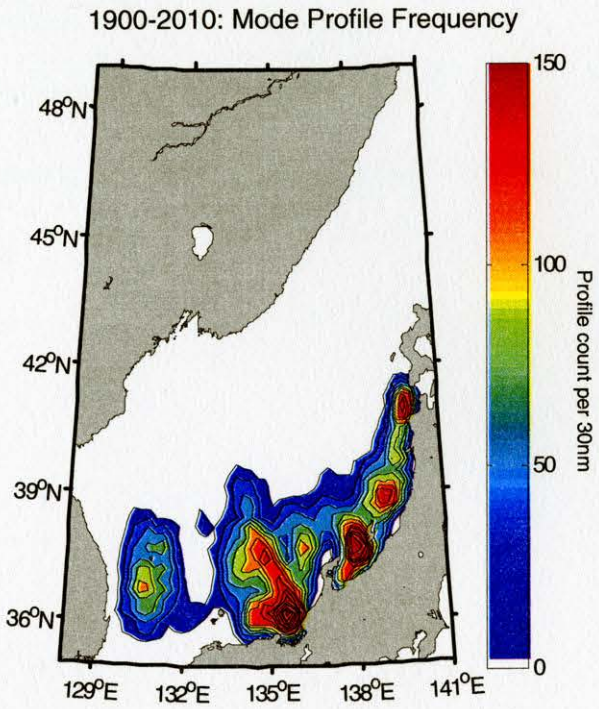

Figure 20. Mode water frequency map of the 1900-2010 dataset. Counts made from 0.5° x 0.5° bins.

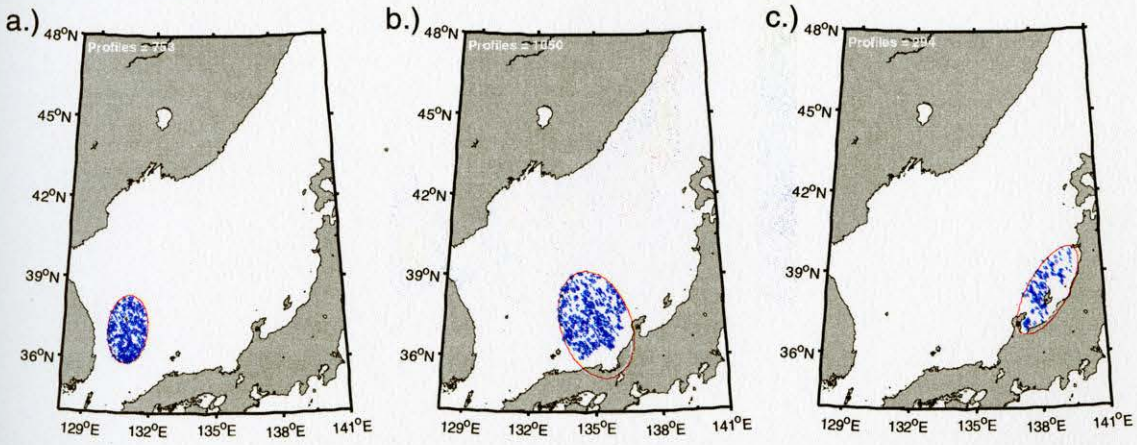

Figure 21. Conductivity-Depth-Temperature (CTD) data retained from the 1900-2010 dataset. Perimeters for each of the ITE ellipses was determined from Fig. 20. (*a*) Profiles retained in the Ulleung ITE, (*b*) profiles retained in the Yamato ITE, and (*c*) profiles retained in the Western Honshu ITE.

4415 profiles identified (Fig. 20), and data from the 40-count contour for the Ulleung, Yamato, and Western Honshu ITEs were fitted to an ellipse. Data from the 1900-2010 dataset located inside these ellipses were retained. Expendable Bathythermographs (XBTs), temperature-depth only profiles, were excluded as further calculations require salinity data (Fig. 21).

CHAPTER V

METHODS

This study made use of two primary data analysis methods, Empirical Orthogonal Function (EOF) analysis and multi-variate least squares regressions. EOF analysis has been shown to be a useful tool for determining synthetic profiles in the past (deWitt, 1987; Carnes et al., 1990, 1994). The EOF method decomposes a dataset in terms of basis functions which are determined by the data. The EOF process is a way of describing as much of the variability of a large dataset in as few basis functions as possible. In this case, a basis function can be interpreted as vertical temperature corrections to a mean temperature profile. A brief outline of the EOF process is given below as it was applied in this study.

All profiles remaining in the ITE ellipse datasets are interpolated to standard depths from the surface to 500m at 1m increments. A bottom depth of 500m is chosen because below this, the waters of the SOJ are very homogenous. A mean temperature profile is then determined and removed from all profiles so only temperature anomalies remain. Any missing data in the upper 20m or lower 50m is filled to the top and bottom with the first/last recorded temperature value of the profile. Profiles missing more than 20m of data in the upper water column and 50m in the lower column are excluded from the analysis. The covariance matrix of the temperature anomalies where k is the profile number, T' is the temperature anomaly, and $z_{i,j}$ is the depth level, given by equation (2), is determined for the dataset.

$$COV(z_i, z_j) = \frac{1}{k}\sum_{k=1}^{k}[T'(z_i,k)][T'(z_j,k)] \qquad (2)$$

Since the covariance matrix is both real and symmetric, eigenvectors (basis functions/EOFs), θ_n, and eigenvalues, λ_n, may be found by solving the eigenvalue problem below, where n is the number of depth levels.

$$\sum_{i=1}^{n} COV(z_i, z_j)\theta_n(z_i) = \lambda_n \theta_n(z_j) \tag{3}$$

The overall variance captured by any particular basis function is determined by the value of its eigenvalue, λ_n, relative to the sum of all eigenvalues which represents the total variance of the dataset (deWitt, 1987). The last step in the EOF process is to determine the basis function amplitudes, A_n, for each profile. The amplitude determines the influence each basis function has on an individual profile.

$$A_n = \sum_{1}^{n} T'(z_i)\theta_n(z_i) \tag{4}$$

All regression analysis utilizes an ordinary least squares method (OLS). OLS is a method used to estimate the unknown coefficients of a regression model (Burden and Faires, 1997). The first step in this process is determining the sum of the squared errors between the observed points and the points predicted by the regression model. The error term, E, is found using equation (5), where N is the number of data points, y_i is the observed value, and $f(x_i)$ is the predicted value from the regression model. Considering the simplest case where $f(x)$ is a linear model, $y=ax+b$, the goal of OLS is to find the values of a and b that minimize the error between true and predicted values. In order to do this, values of a and b must be found such that the equations in (6) hold. Differentiating (6) yields the equations in (7), which may be written in matrix form shown in (8). Since it can be shown that the matrix on the left-hand side of (8) is invertible, both sides of the matrix equation in (8) can be multiplied by inverse of the left-

hand side matrix and rewritten as (9). The best fit values of a and b are obtained by solving the set of linear equations given in (9). General solutions of a and b are shown in equations (10) and (11) (Burden and Faires, 1997).

$$E = \sum_{i=1}^{N} [y_i - (f(x_i))]^2 \tag{5}$$

$$\frac{\partial E}{\partial a} = 0, \frac{\partial E}{\partial b} = 0 \tag{6}$$

$$\begin{aligned} \sum_{i=1}^{N} (y_i - (ax_i + b)) \cdot x_i &= 0 \\ \sum_{i=1}^{N} (y_i - (ax_i + b)) &= 0 \end{aligned} \tag{7}$$

$$\begin{bmatrix} \sum_{i=1}^{N} x_i^2 & \sum_{i=1}^{N} x_i \\ \sum_{i=1}^{N} x_i & \sum_{i=1}^{N} 1 \end{bmatrix} \begin{bmatrix} a \\ b \end{bmatrix} = \begin{bmatrix} \sum_{i=1}^{N} x_i y_i \\ \sum_{i=1}^{N} y_i \end{bmatrix} \tag{8}$$

$$\begin{bmatrix} a \\ b \end{bmatrix} = \begin{bmatrix} \sum_{i=1}^{N} x_i^2 & \sum_{i=1}^{N} x_i \\ \sum_{i=1}^{N} x_i & \sum_{i=1}^{N} i \end{bmatrix}^{-1} \begin{bmatrix} \sum_{i=1}^{N} x_i y_i \\ \sum_{i=1}^{N} y_i \end{bmatrix} \tag{9}$$

$$a = \frac{N(\sum_{i=1}^{N} x_i y_i) - (\sum_{i=1}^{N} x_i)(\sum_{i=1}^{N} y_i)}{N(\sum_{i=1}^{N} x_i^2) - (\sum_{i=1}^{N} x_i)^2} \tag{10}$$

$$b = \frac{(\sum_{i=1}^{N} x_i^2)(\sum_{i=1}^{N} y_i) - (\sum_{i=1}^{N} x_i y_i)(\sum_{i=1}^{N} x_i)}{N(\sum_{i=1}^{N} x_i^2) - (\sum_{i=1}^{N} x_i)^2} \tag{11}$$

First and second order regression models are tested for each characteristic variable, as well as several combinations of input variables. The coefficient of determination, r^2, is used to determine the strength of the regression in predicting mode layer parameters. In this case, the r^2 value is appropriate because it gives the proportion of variance of the observed dataset captured by the regression. Higher order models are only implemented when r^2 values are considerably improved.

CHAPTER VI

RESULTS

Empirical Orthogonal Function (EOF) analysis is performed on the largest ITE data-cluster, the Yamato data (Fig. 22). From the EOF analysis done on the Yamato data, three basis functions (eigenvectors) captured 95% of the dataset variance, with the first basis function alone describing more than 50% of the variability (Fig. 23a). Adding each individual basis function correction to the mean profile shows each function's effect on the profile shape. From Fig. 23b, it is seen that the first basis function acts to uplift or depress the thermocline, while the second and third basis functions are responsible for forming the mode water layer.

However, in order for the EOF analysis to be useful for synthetic recreation, the basis function amplitudes, which determine the importance of the function's correction for each profile, must be correlated to some remotely sensed parameter. In the past, this has been done mainly using dynamic height, which is a proxy for SSH measured by satellite altimetry. Correlating the basis function amplitudes with dynamic height (0/500dbar) computed from the profiles, shows no correlation past the first basis function and no discernable difference between mode and non-mode profiles (Fig. 24).

An alternative parameter of mid-water column stratification was calculated and plotted versus the basis function amplitudes. The stratification parameter is a value calculated for a static depth interval of 100-150m, the general depth mode water occupies, for all profiles in the dataset. This parameter shows far better correlation with all three functions as well as a stratification "threshold" for mode to non-mode profiles (Fig. 25). Since the stratification parameter shows good correlation with all basis

functions, the plots shown in Fig. 25 are also fitted to cubic functions. The regression coefficients for the cubic fit are used to predict the amplitude of each basis function from a single value of stratification so that a synthetic profile can be built. It is seen from Fig. 26 that indeed sliding the stratification number from high to low creates a mode water layer in the synthetic profile. All that is left to show is that this stratification parameter can be tied to some remotely sensed measurement. Although stratification shows correlation between itself and dynamic height, it is a non-linear correlation, and therefore the stratification parameter lacks a unique surface trigger necessary to make the synthetic profiles operational (Fig. 27).

Although the basis functions from the EOF analysis failed to show good correlation with remotely sensed variables, parameterization of the mode layer characteristics could be achieved through correlation and regression with dynamic height

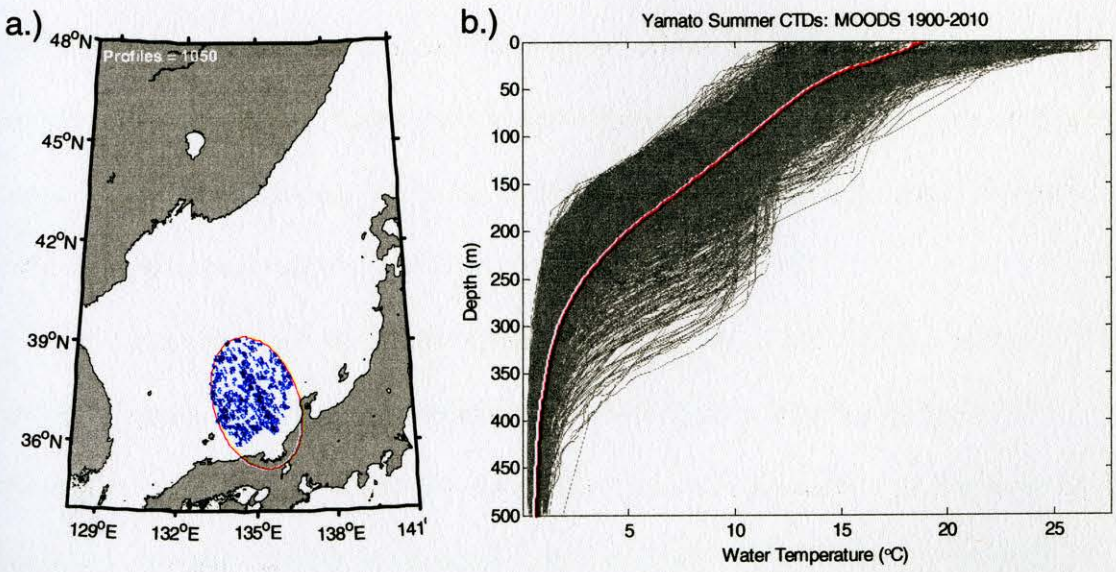

Figure 22. Yamato data used to compute Empirical Orthogonal Functions (EOFs). (*a*) Location map of the 1050 Yamato mode profiles used in the EOF analysis, (*b*) vertical temperature profiles of the 1050 mode profiles used, red profiles depicts the mean temperature of the dataset.

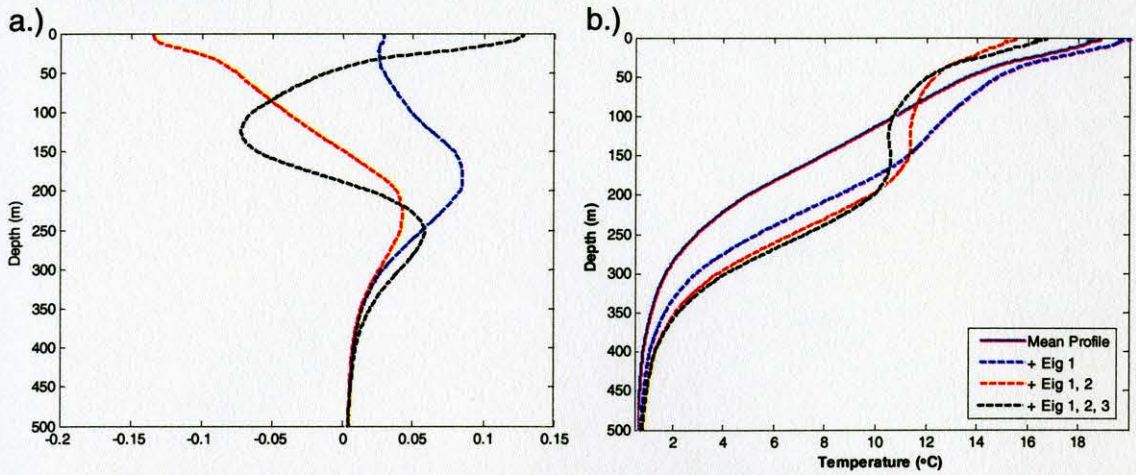

Figure 23. (*a*) Basis functions (Eigenvectors) of the Yamato EOF analysis. The first eigenvector (blue dash) describes 53.1% of the variance, the second eigenvector (red dash) describes 31.6% of the variance, and the third eigenvector (black dash) describes 10.3% of the variance. (*b*) Consecutive addition of the basis function's correction to the mean profile shows the effect each individual basis function on the profile shape.

and sea surface temperature (SST). Fig. 28 shows scatter plots of the first basis function from the EOF analysis versus the dynamic height of only the mode water profiles in the Yamato dataset. It has already been shown that the first basis function controls the movement of the thermocline, so it is no surprise that the first function shows a linear relationship with dynamic height. What is promising, however, is the fact that there also seems to be a signal in mode layer characteristics as well, with positive correlation in mode layer thickness and the bottom of the mode layer (Fig. 28).

First and second-order multi-variate regressions using both surface parameters of SST and dynamic height are determined for the first basis function amplitudes, the bottom of the mode layer, and mode layer thickness. The regression equations for EOF_1 amplitude, the bottom depth of the mode layer, and mode layer thickness are given in (10) – (12), respectively. The known values of SST and dynamic height are denoted by X_1 and X_2, respectively. Predicted variables of EOF_1 amplitude, bottom depth of the

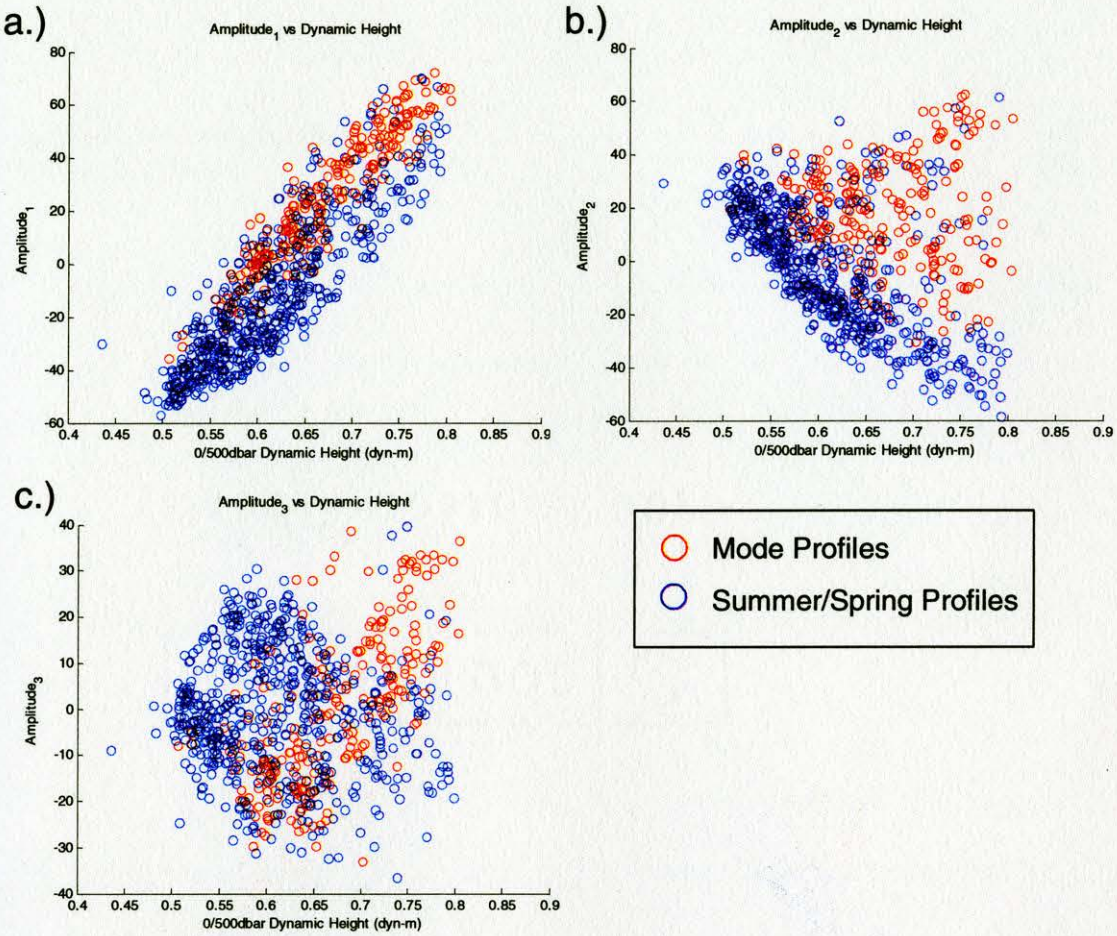

Figure 24. Scatter plots of basis function amplitude and dynamic height (0/500dbar) of the profile. Red circles denote those identified as mode water profiles, and blue circles denote all profiles in the Yamato dataset during mode water peak occurence months. (*a*) Scatter between the first basis function amplitude and profiles dynamic height, (*b*) scatter between the second basis function amplitude and profile dynamic height, and (*c*) scatter between the third basis function amplitude and profile dynamic height.

mode layer, and the mode layer thickness are denoted by Y_1, Y_2, and Y_3, respectively. In this case, both known surface values are taken from the profiles themselves and therefore represent the "best-case scenario" when remotely-sensed measurement errors are at their least.

$$Y_1 = \beta_1 X_1 + \beta_2 X_2 + \beta_0 \qquad (10)$$

$$Y_2 = \alpha_1 Y_1 + \alpha_2 X_2 + \alpha_0 \qquad (11)$$

$$Y_3 = \gamma_1 (Y_2)^2 + \gamma_2 (X_2)^2 + \gamma_3 Y_2 + \gamma_4 X_2 + \gamma_0 \qquad (12)$$

where β, α, and γ represent coefficients

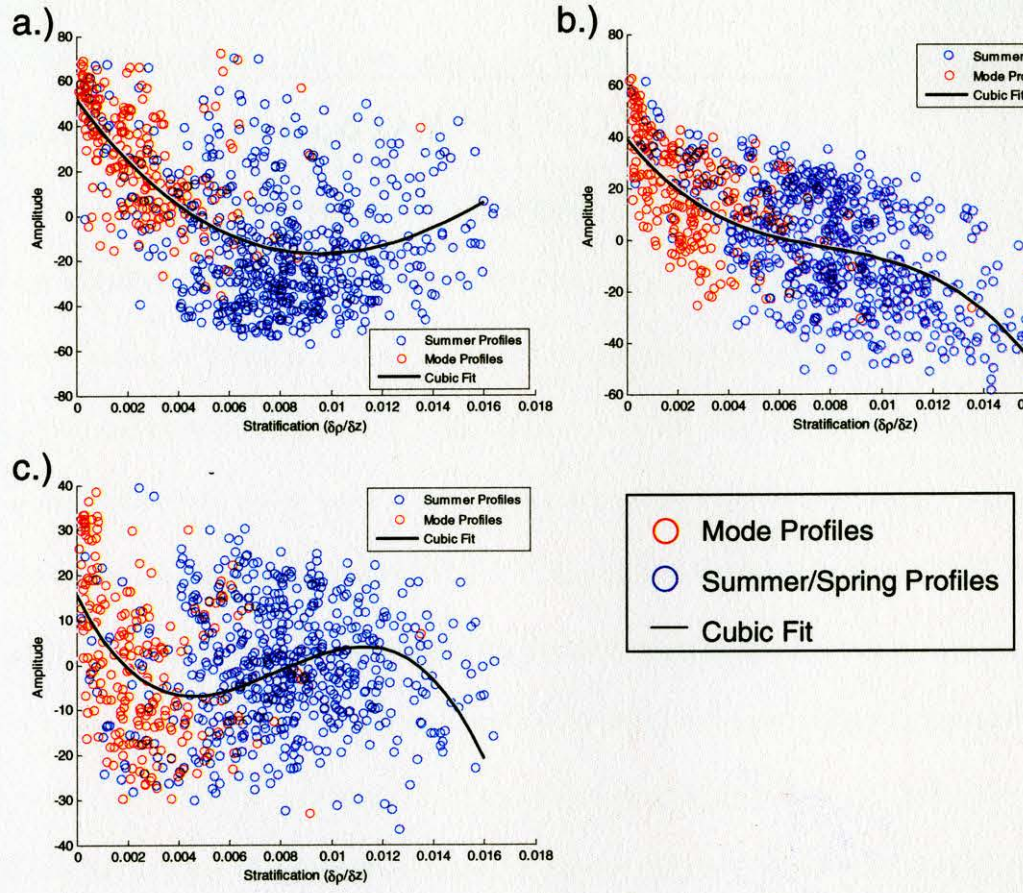

Figure 25. Scatter plots of basis function amplitude and mid-water column stratification of the profile. Stratification parameter determined for all profiles over a static interval of 100-150m. Red circles denote those identified as mode water profiles, blue circles denote all profiles in the Yamato dataset during mode water peak occurrence months, and the black line is a cubic fit of the basis function amplitudes to stratification. (*a*) Scatter between the first basis function amplitude and profiles dynamic height, (*b*) scatter between the second basis function amplitude and profile dynamic height, and (*c*) scatter between the third basis function amplitude and profile dynamic height.

It is seen from Figures 29-31 the predicted values for the variables controlling the shape of the synthetic profile show good correlation with the known values. The

coefficient of determination, r^2, is 0.92 for EOF_1 amplitude lending very high confidence to the prediction of its value from surface parameters. The r^2 values of the variables describing the characteristics of the mode layer are lower, 0.76 and 0.72. However, it is important to note that the points showing the poorest correlations are those with mode layer temperatures farthest from the mean temperature of 10.7°C (Fig. 12). Weighting profiles with atypical mode layer temperature less, correlations between all true and predicted variables rise above 0.90.

Using the regressions given in equations (10)-(12) the mean temperature profile of the dataset is reshaped in order to determine new synthetic profiles. First, the thermocline is adjusted according to the EOF_1 amplitude. Second, the mode water layer is imposed on the profile according to the predicted values of mode layer thickness and bottom depth of the mode layer. The temperature of the layer is modulated within a 0.5°C range around a mean temperature of 10.7°C to mimic natural variability. Third, the mode layer is "smoothed" into the rest of the profile using exponential functions. This is done with a two step process. The temperature values above the mode layer exponentially decrease, according to equation (13), from the surface to the top of the mode layer holding the surface temperature constant. Equation (13) is scaled by the temperature difference between the surface value and that of the mode layer, allowing faster temperature decay for larger offsets. The temperature values below the mode layer exponentially decrease, according to equation (14), from the bottom of the mode layer down 30m holding the bottom-most temperature value constant. Equation (14) is scaled by the temperature difference between the mode layer and that of the temperature value 30m below, again allowing faster temperature decay for larger offsets. Several values of

the decay constant were tested with 0.2 showing the best results. Figure 32 shows the mode layer imposed on the profile before any modifications are made, compared to the corrections described above using the exponential smoothing functions in (13)-(14). Lastly, the entire profile is smoothed several times using a running average filter,

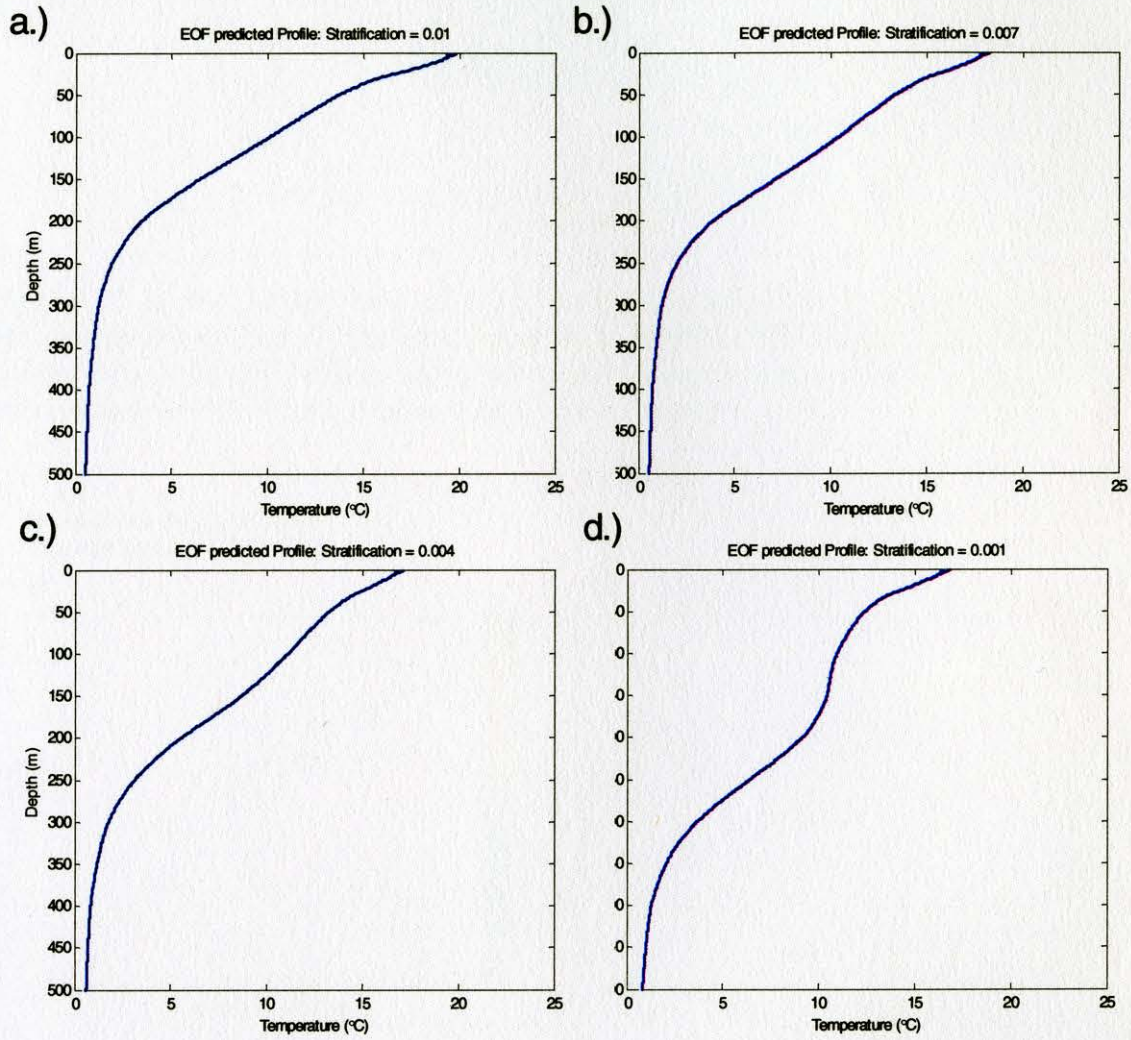

Figure 26. Synthetic profiles created from the regressions correlating basis function amplitude and the stratification parameter. Effect of lowering the stratification number is seen. (a) Synthetic profile created when stratification number is 0.01, (b) synthetic profile created when stratification number is 0.007, (c) synthetic profile created when stratification number is 0.004, and (d) synthetic profile created when stratification number is 0.001.

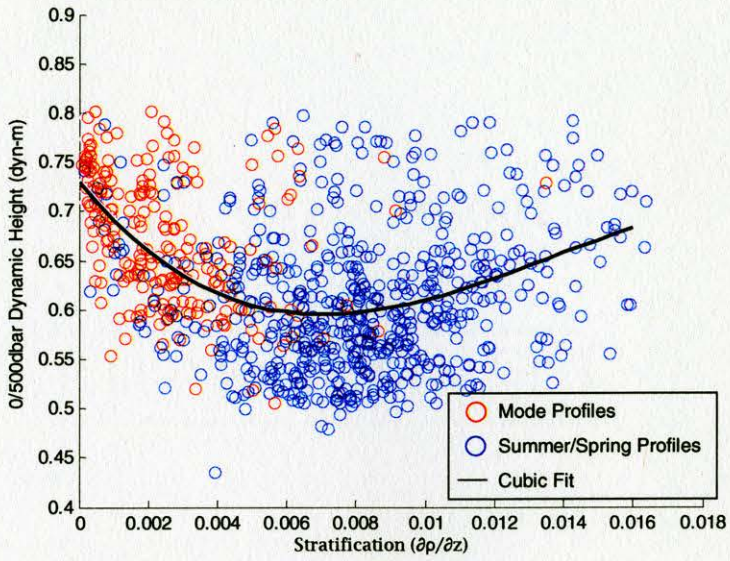

Figure 27. Scatter plot of stratification versus dynamic height of the Yamato dataset. Red circles denote those identified as mode water profiles, blue circles denote all profiles in the Yamato dataset during mode water peak occurrence months, and the black line is a cubic fit of the profile stratification and dynamic height.

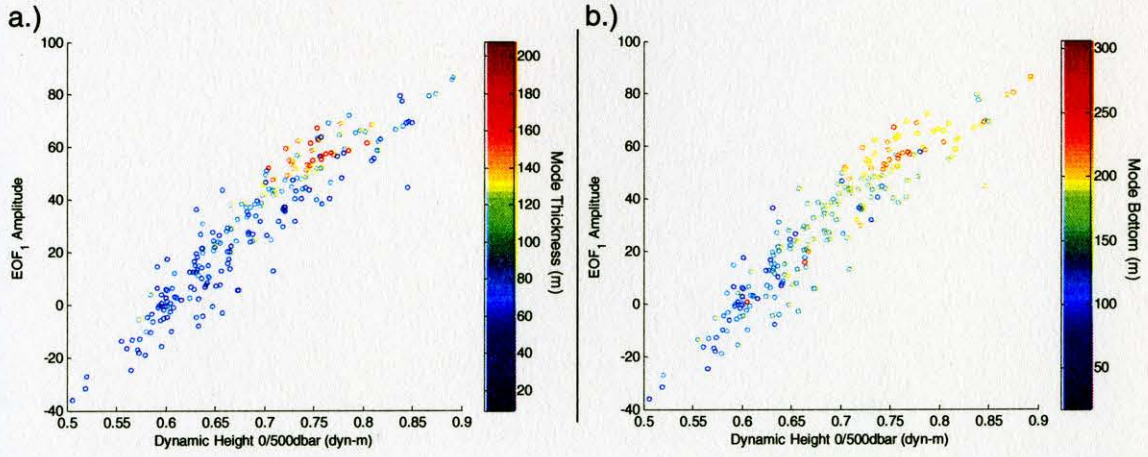

Figure 28. Scatter plots of dynamic height and the amplitudes of the first EOF basis function from the mode water profiles in the Yamato dataset. Colors of the circles denote values of the mode layer characteristics of, (a) mode layer thickness, and (b) the bottom of the mode layer.

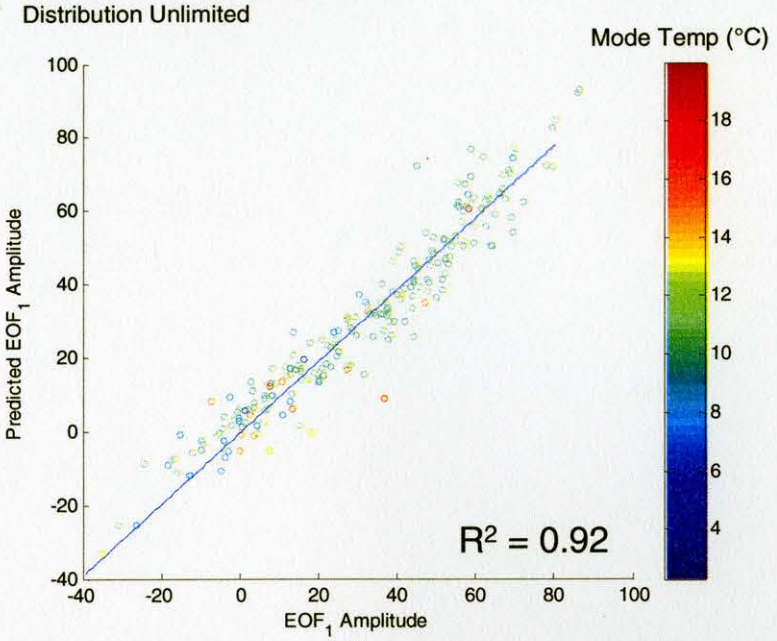

Figure 29. Scatter plot of the EOF_1 amplitude and the predicted EOF_1 amplitude. Done using the regression shown in equation (10). Temperature of the profile's mode layer is shown in the color bar.

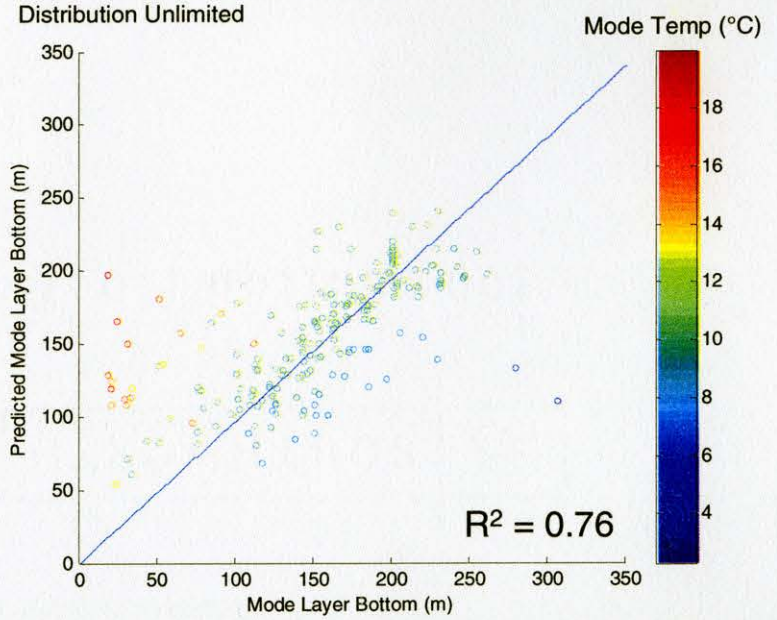

Figure 30. Scatter plot of bottom depth of the mode layer and the predicted bottom depth of the mode layer. Done using the regression shown in equation (11). Temperature of the profile's mode layer is shown in the color bar.

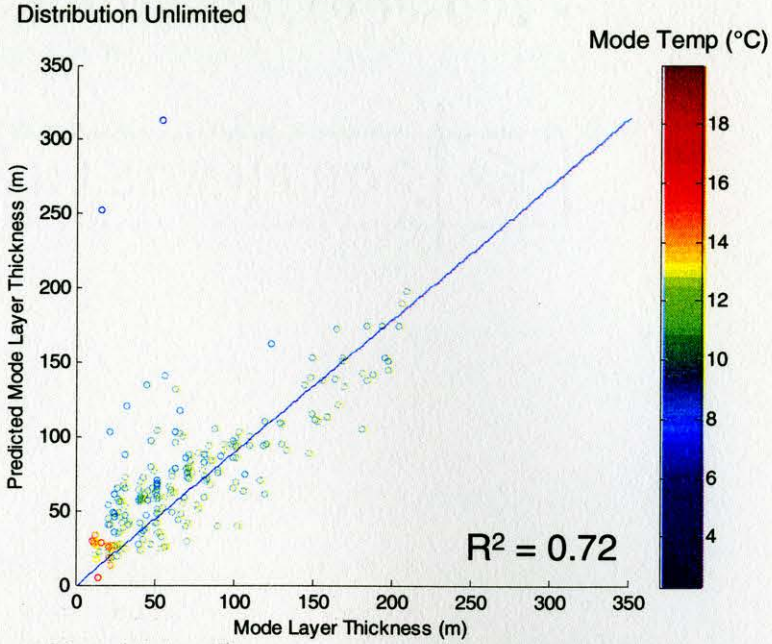

Figure 31. Scatter plot of mode layer thickness and the predicted mode layer thickness. Done using the regression shown in equation (12). Temperature of the profile's mode layer is shown in the color bar.

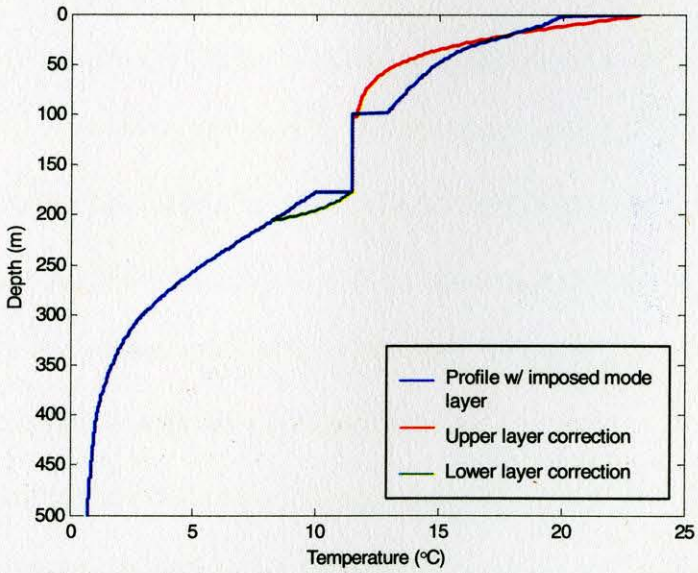

Figure 32. Exponential smoothing corrections done to experimental synthetic profiles. Example of initial synthetic profile with the imposed mode layer before any corrections are done (blue), upper layer exponential correction (red), and lower layer exponential correction (green).

described in equation (15), holding surface and bottom temperature values constant. From Figure 33, it is seen that this process does not adversely affect the profile shape and only eliminates unnatural "jumps" in the temperature gradient.

$$\frac{1}{1+e^{-0.2Z}} \tag{13}$$

$$e^{-0.2Z} \tag{14}$$

$$T_z = 0.5(T_{z-1} + T_{z+1}),\ z=2,3,4...N-1 \tag{15}$$

where T is the temperature, z is the depth level, and N is the number of depth levels

To test the new synthetic method, mode water profiles from 2011 were extracted. Figure 34 shows the 2011 in-situ mode water profiles compared to the current operational synthetics R-NCOM assimilates (near to the in-situ profile in both time and space) as well as the new experimental synthetics derived from the in-situ surface information. It is clear that the operational synthetics do not capture the mode water signature at all, while the experimental synthetics reproduce the in-situ structure well. From the thirty-four mode water profiles from 2011, the mean and standard deviation of the errors between in-situ and synthetic profile were calculated (Fig. 35); it is seen that the experimental synthetics show a far lower mean error in the upper 200m than R-NCOM's operational synthetics with a similar standard deviation in error.

In the general case, however, the new synthetic method does not do an adequate job differentiating between mode and non-mode profiles if the regressions are uniformly applied to the entire ITE ellipse areas for spring and summer months. Figure 36 shows the case if new synthetic profiles are created for any remotely-sensed surface data taken over the Yamato ellipse and their corresponding in-situ profiles from 2011 taken in the

ellipse. It is easily seen that for the mode profiles, the new synthetics do a good job recreating the vertical structure of the profiles. Although some of the new synthetics corresponding to non-mode profiles do indeed lack a mode layer, a false mode layer will be created over much of the area.

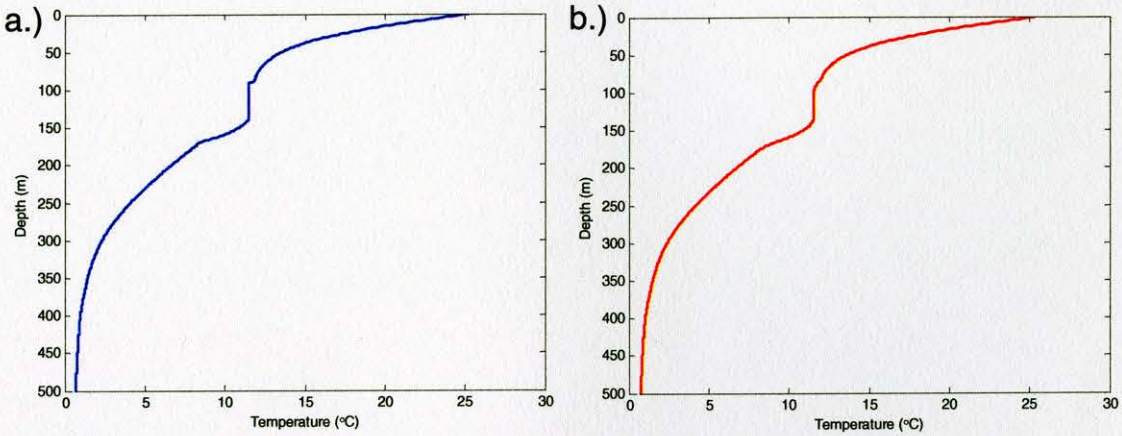

Figure 33. Effect of successively filtering the synthetic profiles. Example synthetic profile before successive moving average filter is applied (a), and the same synthetic profile after the moving average filter is applied (b).

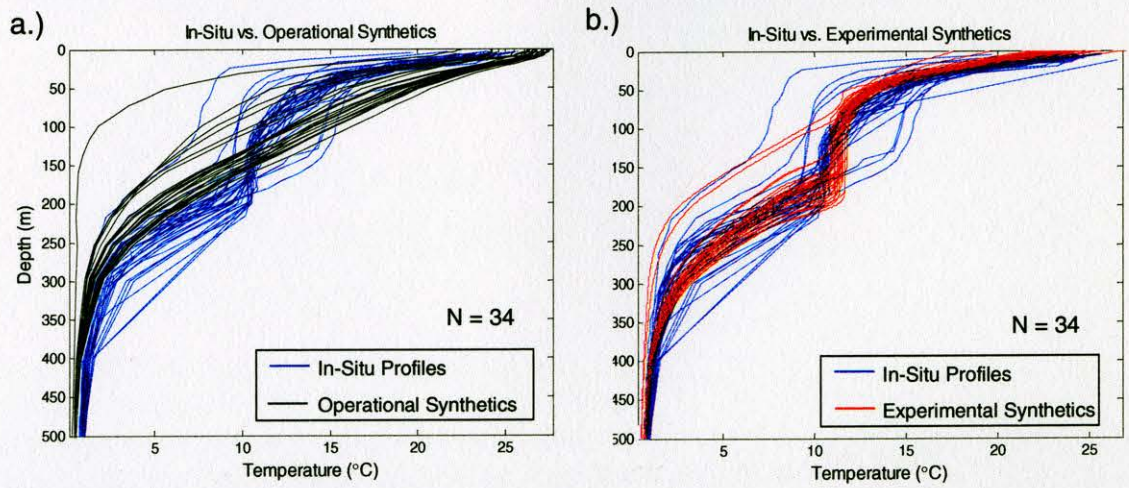

Figure 34. In-situ mode water profles from 2011 compared to operational and experimental synthetic profiles. (a) In-situ mode water profiles from 2011 compared to nearby operational synthetics assimilated by R-NCOM. (b) In-situ mode water profiles from 2011 compared with the experimental synthetics derived from the surface values of the in-situ data.

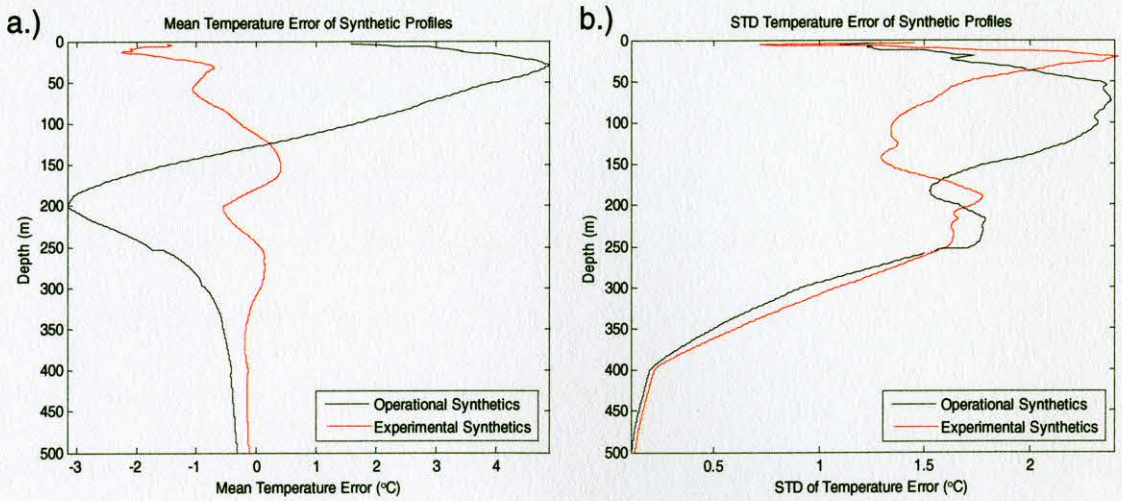

Figure 35. (a) Mean error and (b) standard deviation of error between the in-situ data (red) and operational (black) and experimental (red) synthetics.

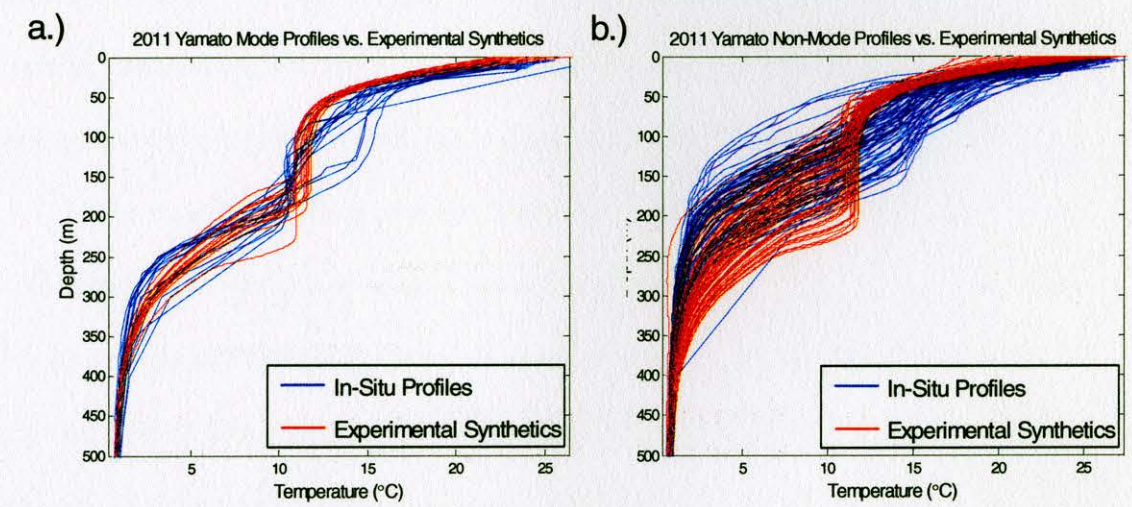

Figure 36. Data taken inside the Yamato ellipse during 2011 compared to experimental synthetic profiles. (a) Mode water profiles taken inside the Yamato ellipse during 2011 (blue) and their corresponding synthetic profiles (red) calculated using the experimental method. (b) Non-mode water profiles taken inside the Yamato ellipse during 2011 (blue) and their corresponding synthetic profiles (red) calculated using the experimental method.

CHAPTER VII

CONCLUSIONS AND DISCUSSION

In the past, the relation of surface measurements to subsurface water column structure has been achieved through the use of EOF analysis (deWitt, 1987, Carnes et al., 1994). While employing the EOF method on a restricted spatial and temporal subset of data in the SOJ is able to produce synthetic profiles that contain a mode water layer, the method fails to show a connection to surface parameters which is vital for placing the synthetics in an operational run-stream. Parameterization of the mode water layer through the use of regression equations relating surface measurements to characteristics of the mode water layer provides a much better avenue, not only allowing for the creation of a mode layer triggered by surface data but also allowing some control over its thickness and placement in the water column. Compared with the operational synthetic profiles currently assimilated into R- NCOM, the experimental synthetics reduce the error associated with mode water presence by more than 20% in the upper water column.

The shortfall of the parameterization method is that is does not do an adequate job differentiating between mode and non-mode profiles if uniformly applied to the ITE ellipse areas prescribed during the peak mode water occurrence months. However, it is believed that the parameterization method may be improved taking into consideration the model's accurate placement of the meander ITE eddies. It was shown in Figure 14, that during 2010, R-NCOM's placement of anti-cyclonic features south of the SPF corresponded very well to the locations of the in-situ mode water profiles taken the same year. The placement of modeled features is heavily influenced by altimetry, and hence

altimetry anomalies may be used to differentiate between the places requiring and not requiring the utilization of the new synthetic method.

With the additional SSH anomaly criterion, the new parameterization method for creating mode water synthetics specifically inside the meander ITEs is hoped to increase R-NCOM's ability to create and retain mode water layers in the SOJ during the spring and summer months. If the new synthetic method is able to be placed into the operational run-stream, this technique could also be applied in the many other places in the world oceans where mode water exists, enhancing modeling capabilities there, as well.

REFERENCES

Burden, R., and J. Faires, 1997, *Numerical Analysis 6th Edition.* Brooks/Cole Publishing Company, Pacific Grove, CA.

Carnes, M., W. Teague, J. Mitchell, 1994, Inference of subsurface thermocline structure from fields measurable by satellite. *J. Atmos. Oceanic Technol,* **11**, 551-566.

Dorman, C., C. A. Friehe, D. Khelif, A. Scotti, J. Edson, R. Beardsley, R. Limeburner, S. Chen, 2006, Winter atmospheric conditions over the Japan/East Sea: The structure of severe cold-air outbreaks. *Oceanography,* **19**, 96-109.

deWitt, P., 1987, Modal decomposition of the monthly Gulf Stream/Kuroshio temperature fields. *NOO Tech. Rep. 298*, 40pp., Nav. Oceanogr. Off., Stennis Space Center, MS.

Fox, D., 2002, The Modular Ocean Data Assimilation System (MODAS). *J. Atmos. Oceanic Technol.,* **19**, 240-252.

Gordon, A., C. Giulivi, C. Lee, H. Furey, A. Bower, L. Talley, 2002, Japan/East Sea Intrathermocline Eddies. *J. Phys. Oceanogr.*, **32**, 1960-1974.

Hanawa, K., and L. Talley, 2001, Ocean Circulation and Climate Observing and Modeling the Global Ocean: Mode Waters. *International Geophysics*, G. Seidler and J. Church, **77**, Academic Press, 373-386.

Hanawa, K., T. Suga, 1995, A review on the subtropical mode water of the North Pacific (NPSTMW), *Biogeochemical Processes and Ocean Flux in the Western Pacific,* H. Sakai and Y. Nozaki, 613-627, Terra Scientific Publishing Company, Tokyo.

Hogan, P., H. Hurlburt, 2006, Why do Intrathermacline Eddies form in the Japan/East Sea. *Oceanography,* **19**, 134-143.

Kostianoy, A., I. Belkin. 1989, Mesoscale/Synoptic Coherent Structures in Geophysical Turbulence: A survey of observations on intrathermocline eddies in the world ocean. *Elsevier Oceanography Series*, J.C.J. Nihoul, 50, 821-841.

Lee, C., L. Thomas, Y. Yoshikawa, 2006, Intermediate water Formation at the Japan/East Sea Subpolar Front. *Oceanography,* **19**, 110-121.

Lunde, B., E. Coelho, 2009, Implementations of the Navy Coupled Ocean Data Assimilation System at the Naval Oceanographic Office, OCEANS '09 Conference, Biloxi, MS, Mar. Tech. Soc.

McCartney, M., 1982, The subtropical recirculation of mode waters. *J. Mar. Res.,* **40**, 427-464.

Mooers, C., H. Kang, I. Bang, D. Snowden, 2006, Some lessons learned from comparisons of numerical simulations and observations of the JES circulation. *Oceanography,* **19**, 86-95.

Morimoto, A., T. Yanagi, A. Kaneko, 2000, Eddy Field in the Japan Sea derived from satellite altimetric data. *J. Oceanogr.,* **56**, 449-462.

Nechaev, D., G. Panteleev, M. Yaremchuk, 2005, Reconstruction of the circulation in the limited region with open boundaries: climatic circulation in the Tsushima Strait. *Oceanology,* **45**, 805-828.

Perkins, H., W. Teague, G. Jacobs, K. I. Chang, and M. Suk, 2000, Currents in Korea/Tsushima Strait during summer 1999. *Geophys. Res. Lett.,* **27**, 3033-3036.

Pond, S., and Pickard, G., 1983, *Introductory Dynamical Oceanography. Elsevier Butterworth-Heinemann*, Kidlington, Oxford.

Preller, R., P. Hogan, 1998, *The Sea. Oceanography of the Sea of Okhotsk and the Japan/East Sea.* **11**, 429-481, *John Wiley and Sons, Inc*, New York, NY.

Price, J., 2001, Ocean Circulation and Climate Observing and Modeling the Global Ocean: Subduction. *International Geophysics*, G. Seidler and J. Church, **77**, Academic Press, 357-371.

Spall, M., 1995, Frontogenesis, subduction, and cross-front exchange at upper ocean fronts. *J. Geophys. Res., C,* **100**, 2543-2557.

Stommel, H., 1979, Determination of water mass properties of water pumped down from the Ekman layer to the geostrophic flow below. *Geophysics,* **77**, 3051-3055.

Talley, L., V. Lobanov, A. Salyuk, P. Tishchenko, I. Zhabin, 2003, Deep convection and brine rejection in the Japan Sea. *Geophys. Res. Lett.,* **30**, 1159-1162.

Williams, R., 1989, The influence of air-sea interaction on the ventilated thermocline. *J. Phys. Oceanogr.,* **19**, 1255-1267.

Xu, Y., D. Watts, M. Wimbush, J. Park, 2007, Fundamental-mode basin oscillations in the Japan/East Sea. *Geophys. Res. Lett.,* **34**, L04605.

Xu, Y., D. Watts, J. Park, 2008, De-Aliasing of large-scale high-frequency barotropic signals from satellite altimetry in the Japan/East Sea. *J. Atmos. Oceanic Technol.,* **25**, 1703-1709.